Journal of the Indian Chemical Society 98 (2021) 100225

Contents lists available at ScienceDirect

Journal of the Indian Chemical Society

journal homepage: www.editorialmanager.com/JINCS/default.aspx

Transition metal incorporated, modified bismuth oxide (Bi_2O_3) nano photo catalyst for deterioration of rosaniline hydrochloride dye as resource for environmental rehabilitation

Prashant Bhimrao Koli [a], Sachin Girdhar Shinde [b,*], Kailas Haribhau Kapadnis [c], Anita Parashram Patil [d], Madhukar Panditrao Shinde [e], Subhash Dharmraj Khairnar [f], Dipti Bhikan Sonawane [c], Raju Shivaji Ingale [g]

[a] Department of Chemistry, Karmaveer Abasaheb and N. M. Sonawane Arts, Commerce and Science College, Satana, Taluka- Baglan, District-Nashik 423301, India[1]
[b] Department of Chemistry K. V. N Naik Arts, Commerce and Science College, Canada Corner, Nashik 422002, India[2]
[c] Research Centre in Chemistry and P G Department of Chemistry, Loknete Vyankatrao Hiray Arts, Science and Commerce, College, Panchavati, Nashik-422003, India[3]
[d] Research Centre in Zoology and P G Department of Zoology, Loknete Vyankatrao Hiray Arts, Science and Commerce, College, Panchavati, Nashik-422003, India[4]
[e] Research Centre in Chemistry and P G Department of Chemistry, K.T.H.M. College, Gangapur Road, Nashik, India[5]
[f] Nano Chemistry Research Laboratory, G. T. Patil, Arts, Commerce and Science College, Nandurbar, Maharashtra, 425412, India[6]
[g] Department of Physics, MITWPU School of Polytechnic and Skill Development, Shivtirthnagar, Kothrud, Pune, 411038, India[7]

ARTICLE INFO

Keywords:
Modified Bi_2O_3 catalyst
R-HCl degradation
Environmental rehabilitation
BET
ROS scavenging Study

ABSTRACT

The work presented here deals with the fabrication of bare Bi_2O_3 and modified Bi_2O_3 photocatalyst. The Bi_2O_3 material was modified with selected transition metals Co^{2+}, Ni^{2+} with the 1% and 3% atomic weight percent insitu doping method via co-precipitation strategy. These three catalysts were successfully utilized for the waste water purification via photocatalytic degradation route. These all fabricated materials were precisely characterized by characterization techniques such as XRD, SEM, TEM, BET, IR and UV-DRS. The characterization techniques reveal the successful synthesis of material and effective modification of bismuth oxide lattice. Since, surface area for modified Bi_2O_3 was found to be enhanced in comparison to the bare Bi_2O_3, as well as declined band gap energy for modified Bi_2O_3 clearly indicates the successful doping of Co^{2+}, Ni^{2+} metals. The bare Bi_2O_3 and modified Bi_2O_3 catalyst were employed for photocatalytic degradation of cationic dye R-HCl dye. The modified Bi_2O_3 found to be excellent over degradation efficiency of R-HCl with almost 97% of dye degradation in comparison to the bare Bi_2O_3. Reactive oxygen species experiment demonstrate that the addition of isopropyl alcohol (IPA), benzoquinone (BQ) and EDTA found to be successful to quench $^{\cdot}OH$, $O_2^{\cdot-}$ and h^+ in photocatalysis mechanism. Additionally, the modified Bi_2O_3 was employed for phenol molecule degradation to investigate the possible excitation of this molecule under visible light irradiation.

1. Introduction

In the recent times, semiconductor photocatalysts have been employed extensively for the environmental remediation. The usability of photocatalyst is remarkable journey in the field of photodegradation of organic pollutants or contaminants for the purification of water [1]. TiO_2 and ZnO based semiconductors are most studied heterogeneous semiconductor considered as an ideal material for photocatalysis attributed to

* Corresponding author.
E-mail address: sachings93@gmail.com (S.G. Shinde).
[1] Affiliated to Savitribai Phule Pune University, Pune (MH), India.
[2] Affiliated to Savitribai Phule Pune University, Pune (MH), India.
[3] Affiliated to Affiliated to Savitribai Phule Pune University, Pune (MH), India-422003.
[4] Affiliated to Affiliated to Savitribai Phule Pune University, Pune (MH), India-422003.
[5] Affiliated to Savitribai Phule Pune University, Pune (MH), India-422003.
[6] Affiliated to Kavayitri Bahinabai Chaudhari North Maharashtra University, Jalgaon (MH), India.
[7] Affiliated to AICTE, Mumbai, (MH), India.

https://doi.org/10.1016/j.jics.2021.100225
Received 27 August 2021; Received in revised form 4 October 2021; Accepted 25 October 2021

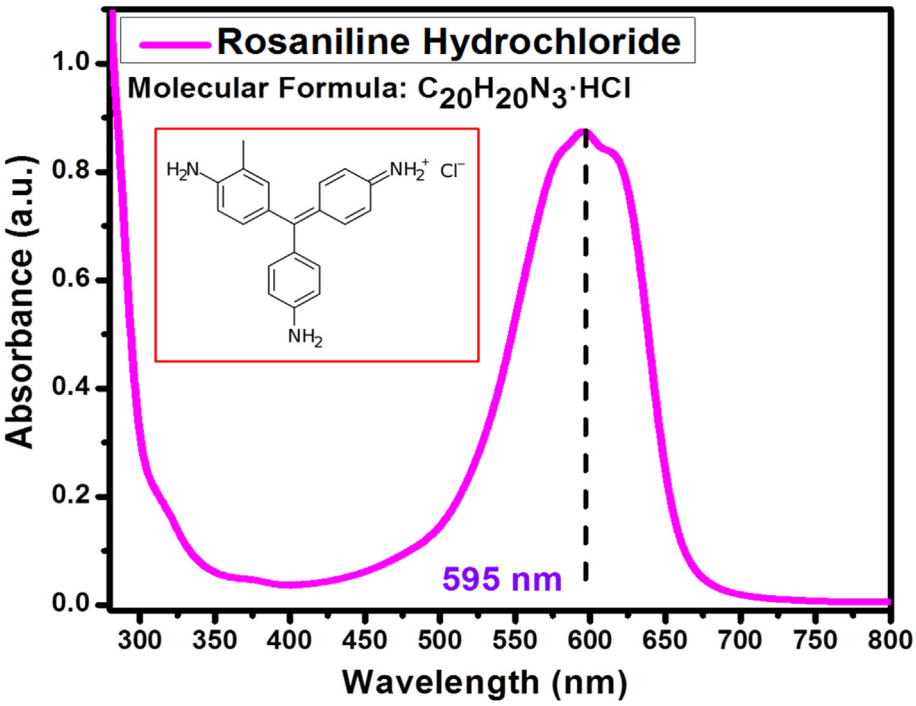

Fig. 1. Characteristics of Rosaniline hydrochloride organic dye.

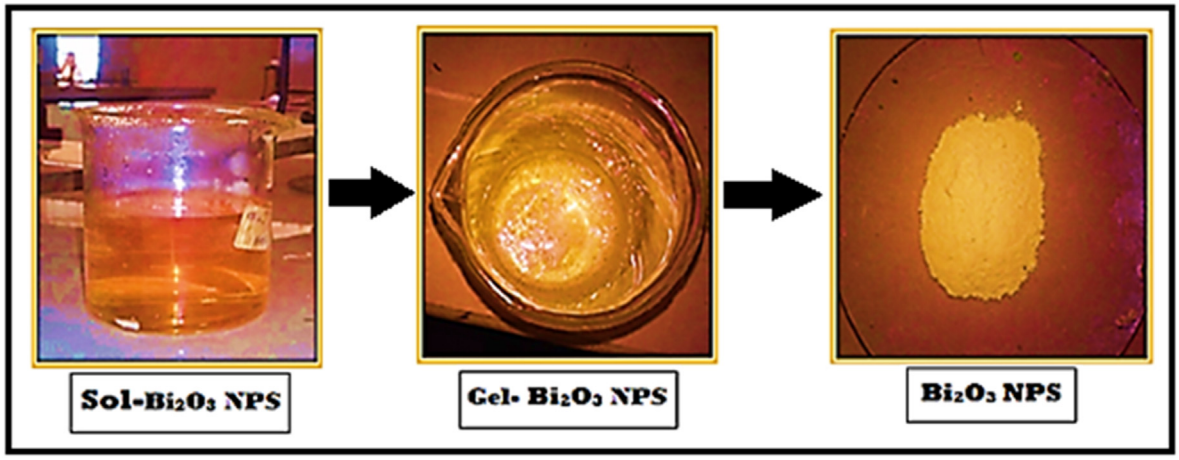

Fig. 2. Bismuth oxide (Bi_2O_3) nanoparticles fabrication by sol-gel strategy.

their abundance, stability, lower toxicity and easy fabrications methods [2,3]. However, due to their large band gap energy (TiO_2 -3.2 eV and ZnO −3.3 eV) consequently less absorption of UV light and rapid recombination of electron and hole photo generated charge carriers (e^-/h^+) impose the scope for the improvement in titania and zinc systems and searching for other semiconducting photocatalysts [4,5]. Metals and non-metals doping in semiconductor to improve the effectiveness practiced all over the world. The transition of ineffective and less effective metal oxide to useful material is achieved by doping. However, many workers are focusing on other material effective than the first generation semiconductors in comparison to the traditional semiconductor photocatalyst [6,7].

The oxides of bismuth are extensively used in coating due to their remarkable optical properties. However; it is attracting to many researchers belonging to the environmental catalysis. Main purpose of this affinity of researchers for bismuth oxide based catalysts is due to its strength, less toxicity and lower band gap energy (2.8 eV). Moreover, Bi_2O_3 is a p-type of semiconductor capable of producing appreciable amount reactive oxidizing species (ROS) like superoxide ($O_2^{\bullet -}$) and hydroxide radical (·OH) in the water medium [8,9]. The bismuth oxide originated catalyst have been reported in many places for their excellent degradation ability towards organic contaminants like dyes, phenols, smaller organic molecules and chlorinated aromatic hydrocarbons [10–12]. However, the Bi_2O_3 having lower band gap energy and lower reduction capacity of oxygen drastically maximize the recombination rate of photo-generated e^- and h^+ after absorption of light [13]. Semiconductor surface can be improved for the oxygen reduction capacity by employing variety of strategies among them doping is widely used and easier option. Significant improvement is evident from many work related to the modification in TiO_2 and ZnO semiconductors by doping of suitable metal doping [13,14].

Transition metal modification is extensively reported in the case of TiO_2 and ZnO. Moradi et al. [15] have confirmed that the Fe doped TiO_2 exhibited efficient photocatalytic performance for the degradation of

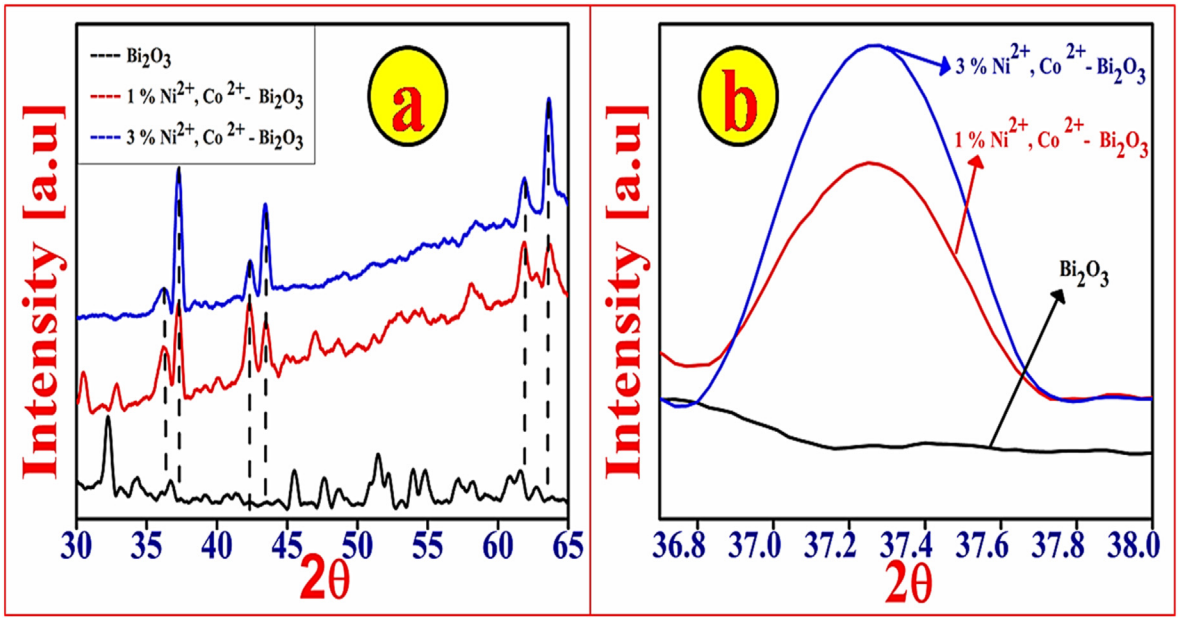

Fig. 3. (a) XRD patterns of the Bi_2O_3 nanoparticles with different Ni^{2+} and Co^{2+} concentrations (b) The enlarged diffraction peaks of the samples with different Ni^{2+} and Co^{2+} concentrations.

Table 1
The lattice parameters of undoped Bi_2O_3, 1% and 3% Ni^{2+}, Co^{2+} Bi_2O_3 nanoparticles.

Sr.	Catalyst	2θ Degree	FWHM(β)	Crystallite Size (nm)
1	Undoped Bi_2O_3	36.59	0.575	15.21
		36.71	0.171	51.16
		40.7	0.327	27.06
		41.45	0.355	24.99
		Average Crystallite Size		29.61
2	1% Ni^{2+}, Co^{2+} Bi_2O_3	36.17	1.190	7.34
		37.25	0.641	13.65
		42.32	1.078	8.26
		43.46	1.409	6.34
		Average Crystallite Size		8.90
3	3% Ni^{2+}, Co^{2+} Bi_2O_3	36.23	1.08731	8.04
		37.28	0.54365	16.12
		42.35	0.79762	11.16
		43.46	0.63604	14.05
		Average Crystallite Size		12.34

methyl orange dye attributed its surface property and lower (3.00 eV) band gap energy. Similarly, Liu et al. [16] used same dopant in ZnO semiconductor and confirmed the improved photodegradation of methylene blue dye. The workers credited the efficiency to the reduction of band gap up to 3.15 eV which is less than pure ZnO. Many such an examples are reported which suggest the improvement of absorption due to reduction of band gap energy after doping. The transition metal dopants form a band near conduction band in a metal oxide and create a convenient path for energetic electron to enter in to conduction band [17,18]. Metal oxides like Bi_2O_3 promotion of electron is faster due to lower band gap however, recombination is also rapid [19]. This drawback is countered by adding dopants which restrict the electron to recombine with hole. The exact continuum which is formed near conduction band traps the electron in it and drastically decrees e^-/h^+ recombination [20,21]. The dopants can also multi task to increase the strength and reusability of semiconductor metal oxide with surface improvement and particle size alteration [22,23]. Due to these peculiarities doping becomes an excellent method for the improvement of less efficient semiconducting materials. More recently the semiconducting oxide based materials are design in the form modified material like Bi_2WO_6 [24], $ZnSnO_3$ [25], ZnO-SnO_2-Zn_2SnO_4 [26], PDI/r-GO [27] $ZnSnO_3$/graphene aerogel [28] etc. are extensively used in the water purification based applications like photocatalysis, adsorptive removal of drugs, dyes and textiles waste effluent water and some other prime applications.

The Bi_2O_3 (Bismuth oxide) is very excellent and facile catalyst used in the various fields of catalysis by the researchers. It has a moderate band gap (approximately 2.5 eV), good surface area and good thermal stability that can be worthy points for this material to be used as a photocatalyst. In broad manner the material undoped Bi_2O_3 frequently used in various catalytic process by the researchers. Hence, in this research we tried to modify the bare Bi_2O_3 by transition metal Co(II) and Ni(II). Due to this multidoping of transition metals some structural, electronic and surface area modification can be seen in the Bi_2O_3 material. Since, the surface area was observed to be increase from 55.12 m^2/g (for bare Bi_2O_3 material) to 80.30 m^2/g (for 3% Co^{2+}, Ni^{2+} doped Bi_2O_3 material), additionally, the energy band gap of the material was also found to be declined for 3% Co^{2+}, Ni^{2+} doped Bi_2O_3 material (shown in Fig. 10) in contrast to the bare Bi_2O_3 material. Hence, these modifications definitely found to be excellent in the photo catalytic degradation experiment. So, it can be say that the modified bismuth oxide is good alternative for these types of applications. In addition to this, the Rosaniline Hydrochloride (R.HCl) photocatalysis is not reported with Bismuth oxide catalyst. Hence, the novelty of this work is can be seen in the form of no reports of R-HCl degradation with modified bismuth oxide based catalysts. Thus, all the characteristics changes for modified bismuth oxide in comparison to the bare bismuth oxide are attributed to successful doping of the transition metals over the bismuth oxide lattice. Due to tuning in band gap, enhanced surface area, slight structural modification, successive electron hole pair generation responsible for effective photocatalytic degradation of R-HCl (nearly 97%) dye with Co^{2+}, Ni^{2+} doped Bi_2O_3 catalyst, which reflects the worthy and novel report for R.HCl dye degradation by modified bismuth oxide catalyst.

2. Materials and methods

All the chemicals in this research are AR grade, purchased from Loba Chemie Mumbai and used without further purification. Chemicals used are bismuth nitrate pentahydrate (Bi $(NO_3)_3.5H_2O$), cobalt chloride hexa-hydrated ($CoCl_2.6H_2O$), Nickel Chloride hexahydrate ($NiCl_2.6H_2O$), Rosaniline Hydrochloride dye (R-HCl), citric acid, sodium

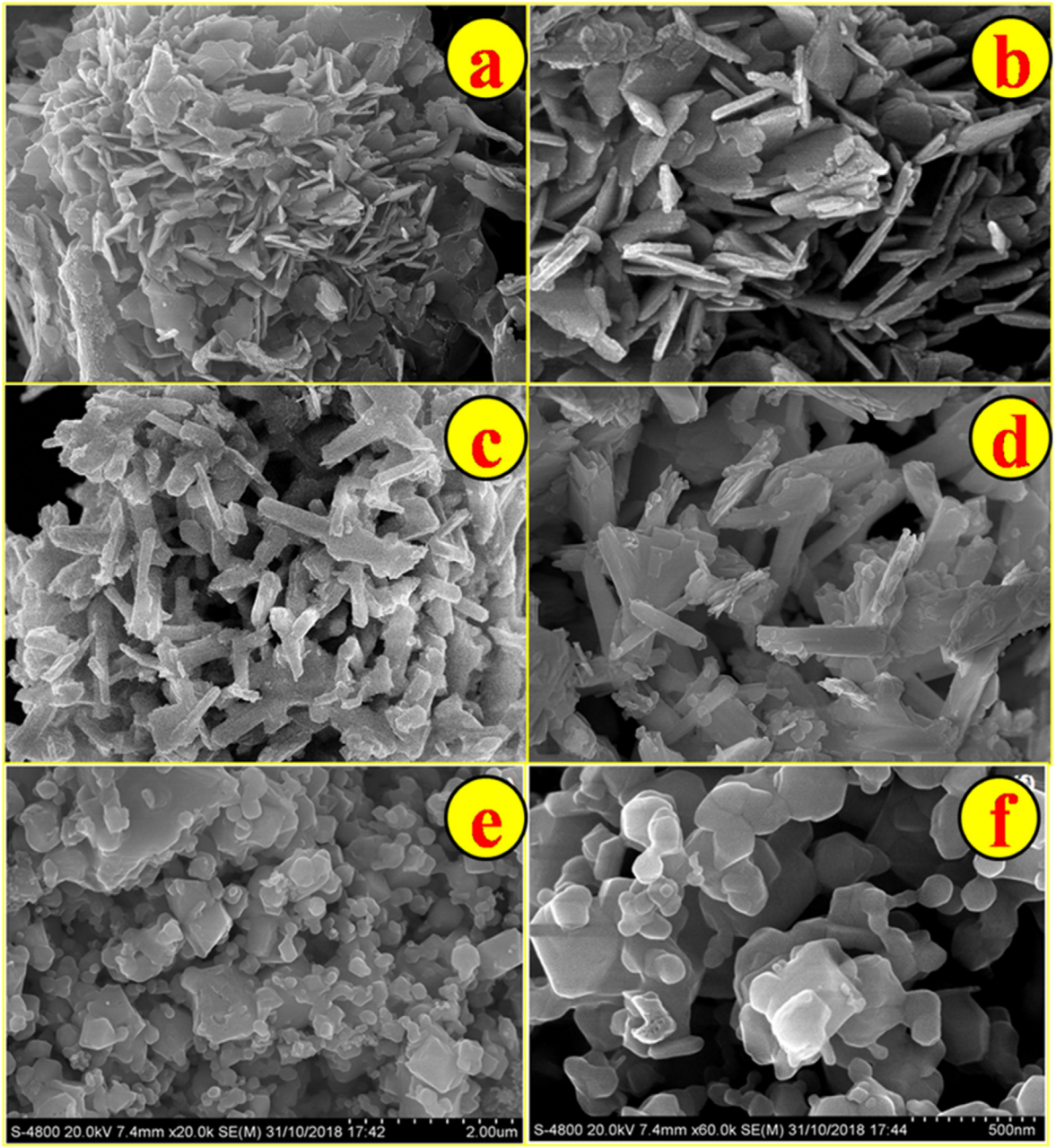

Fig. 4. FE-SEM images of bare Bi_2O_3 (a, b); 1% Ni^{2+}, Co^{2+} doped Bi_2O_3 (c, d) and 3% Ni^{2+}, Co^{2+} doped Bi_2O_3 nanoparticles (e, f).

sulphate, Ammonia, double distilled water.

2.1. Synthesis of Bi_2O_3 nanoparticles by sol-gel route

Bismuth nitrate and citric acid were used for the preparation of Bi_2O_3 are of AR grade 4.65g of $Bi(NO_3)_3.5H_2O$ dissolved in 50 ml concentrated nitric acid and it was mixed with 1.92g of citric acid (0.01 mol) in 1:1 M ratio (Bismuth nitrate and citric acid). Since there was no precipitation during mixing, the pH of solution not varied. The above solution stirred for few minutes and then sol formed. The sol solution was heated to 100 °C on water bath for 3–4 h; yellowish gel was formed after evaporation of water. Direct heating decomposed this gel. The gel initially started to swell and filled to the beaker producing a foamy precursor. This foam consists of homogeneous flakes of very small particle size and after calcinations for 5 h at 550 °C. Yellow powder of bismuth oxide was obtained. After sonication 2.3g of bismuth oxide nanoparticles were isolated [29,30] (see Fig. 1).

The Schematic of sol-gel synthesis of Bi_2O_3 is as shown in Fig. 2.

2.2. Synthesis of 1% Co^{2+}, Ni^{2+} incorporated bismuth oxide (Bi_2O_3) nanoparticles by co-precipitation method

In 50 ml of double distilled water 0.01 M of bismuth nitrate was added, then 25 ml of 0.07 M sodium sulphate was taken in a separate beaker, both these solutions were mixed. To this cumulative solution of bismuth and sodium sulphates the, stoichiometric, calculated amount of dopant concentration of transition metals Co^{2+}, Ni^{2+} precursors was added. The whole solution then stirred at room temperature for 45 min. Then 0.01 M sodium hydroxide solution was dropped in the solution with constant stirring on magnetic stirrer. After complete addition of NaOH (50 ml), a black colored precipitate was obtained, which was filtered, dried and calcined in muffle furnace at 400–500 °C for 4 h. Gray colored Co^{2+}, Ni^{2+} doped Bi_2O_3 nanoparticles were recovered from silica crucible on next day [31,32].

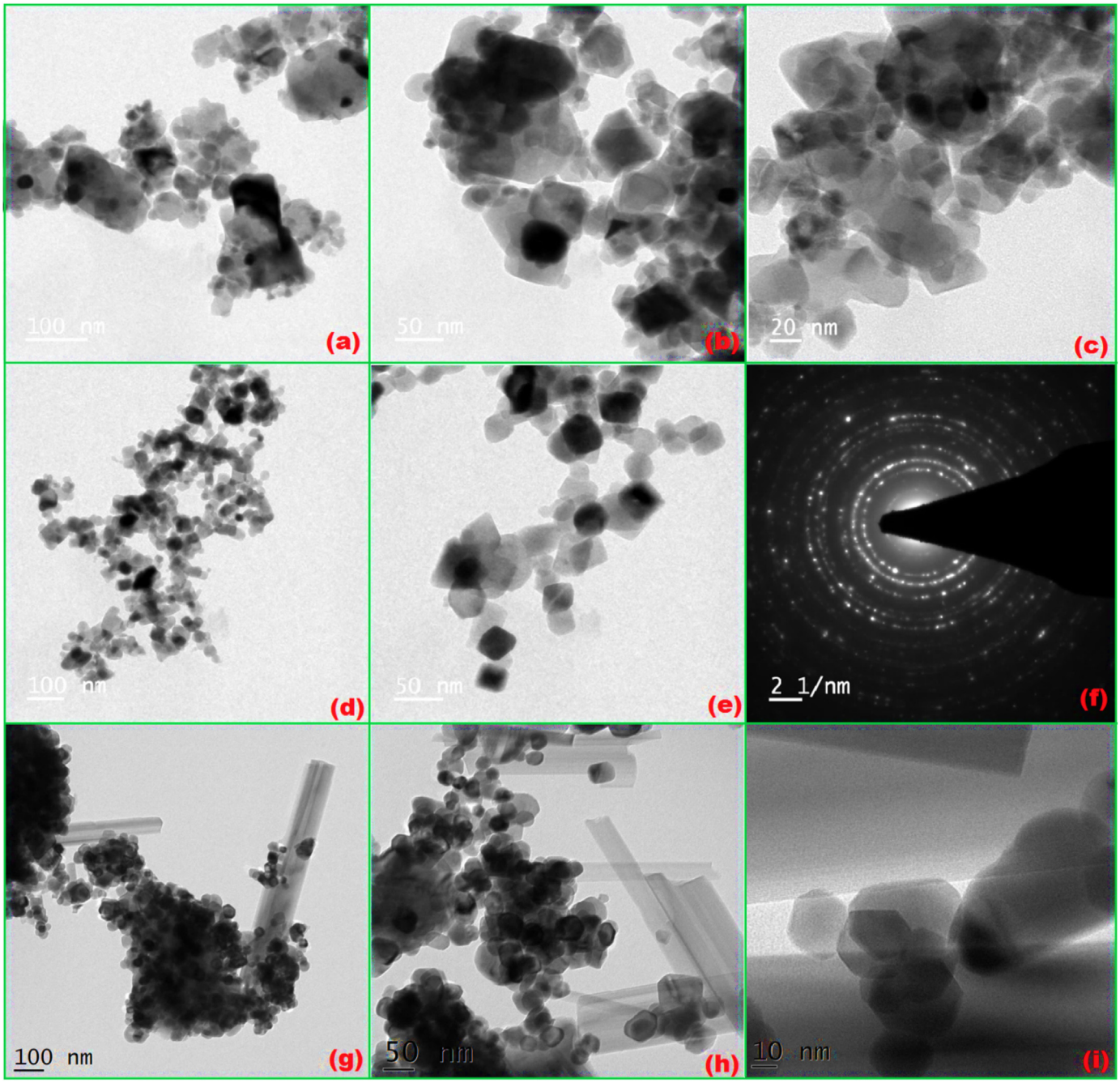

Fig. 5. (a, b, c) TEM images of Bi_2O_3 nanoparticles TEM images, (d, e, f) TEM images and SAED pattern of 1% Ni^{2+}, Co^{2+} doped Bi_2O_3 nanoparticles, (g, h, i) TEM 3% Ni^{2+}, Co^{2+} doped Bi_2O_3 nanoparticles.

2.3. Synthesis of 3% Co^{2+}, Ni^{2+} incorporated bismuth oxide (Bi_2O_3) nanoparticles by co-precipitation method

(The same method as mention in section 2.2 was used to prepare 3% Co^{2+}, Ni^{2+} incorporated Bismuth oxide (Bi_2O_3) nanoparticles. Only the dopant ratio of cobalt and nickel was altered to 3% (atomic weight %)

3. Results and discussions

3.1. Characterization techniques

The X-ray diffraction (XRD) study of the fabricated material Bi_2O_3 and 1%, 3% Co^{2+}, Ni^{2+} modified Bi_2O_3 was characterized by using D8 advance Bruker AXS GmbH (Germany),Bragg's scanning angle varying from 10-80^0. The surface morphology and topographic properties, surface characteristics were investigated by means of Field emission scanning electron microscope (FE-SEM), model number S-4800 type II high technologies corporation, Japan. While the elemental composition of the fabricated materials Bi_2O_3 and 1%, 3% CO^{2+}, Ni^{2+} modified Bi_2O_3 was investigated by using energy dispersive x-ray spectroscopy (EDAX) spectrometer model number X-Flash detector 5030, make Bruker AXS, GmbH, Germany. The lattice morphology, crystalinity, surface properties were investigated by means of high resolution transmission electron microscope (HR-TEM), model number Jeol/JEM, having 200 kV operational range, LaB6 electron gun with lattice resolution of 0.14 nm and point resolution 0.23 nm provides additional selected area diffraction pattern (SAED) information. Additionally, the material was characterized by Brunauer-Emmett-Teller (BET) study with N_2 adsorption-desorption

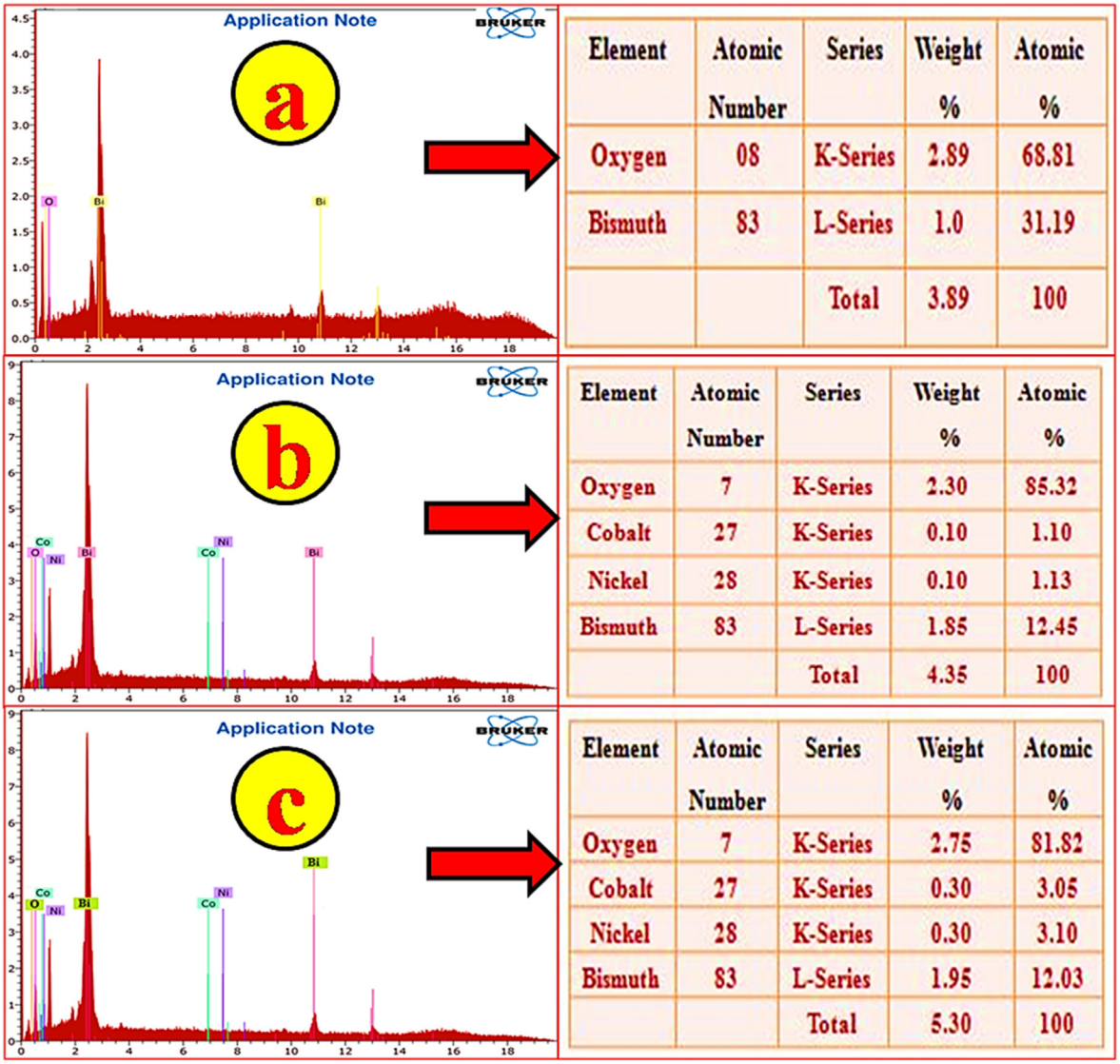

Element	Atomic Number	Series	Weight %	Atomic %
Oxygen	08	K-Series	2.89	68.81
Bismuth	83	L-Series	1.0	31.19
		Total	3.89	100

Element	Atomic Number	Series	Weight %	Atomic %
Oxygen	7	K-Series	2.30	85.32
Cobalt	27	K-Series	0.10	1.10
Nickel	28	K-Series	0.10	1.13
Bismuth	83	L-Series	1.85	12.45
		Total	4.35	100

Element	Atomic Number	Series	Weight %	Atomic %
Oxygen	7	K-Series	2.75	81.82
Cobalt	27	K-Series	0.30	3.05
Nickel	28	K-Series	0.30	3.10
Bismuth	83	L-Series	1.95	12.03
		Total	5.30	100

Fig. 6. EDS image of Pure Bi_2O_3 nanoparticles (a); 1% Ni^{2+}, Co^{2+} doped Bi_2O_3 nanoparticles (b); 3% Co^{2+}, Ni^{2+} doped Bi_2O_3 nanoparticles (c).

experiment to investigate the surface area of the fabricated materials by Quanta chrome Autosorb 1C BET Surface Area & Pore Volume Analyzer. The optical and band gap properties were analyzed by using ultraviolet differential reflectance spectroscopy (UV-DRS) equipment model UV Vis NIR Spectrophotometer Agilent Cary 200 nm–3000 nm. The metal oxide vibrational frequencies were investigated by means of Fourier transform infra-red spectroscopy (FT-IR).

3.2. X-ray diffraction (XRD) study

In order to investigate the phase structure, the XRD patterns of pure and doped Bi_2O_3 with different Ni^{2+} and Co^{2+} concentrations were analyzed. As a representative example XRD pattern of undoped Bi_2O_3 and Ni^{2+} and Co^{2+} doped Bi_2O_3 is shown in Fig. 3(a). The results indicate that the phase structure changed upon doping. The dopant can enter the Bi_2O_3 lattice either interstitially or it can act as substitution impurity. In the present case the ionic radius of Ni^{2+} and Co^{2+} is (70 p.m.) and that of Bi^{3+} is (103 p.m.). The ionic radius of Ni^{2+} and Co^{2+} (70 p.m.) are significantly smaller than the Bi^{3+} therefore, it is difficult for the Ni^{2+} and Co^{2+} to act as surface impurity, but it may be present in the interstitial position in Bi_2O_3 lattice. The average crystallite sizes of pure and doped Bi_2O_3 nanoparticles were determined by Debye Scherer formula Equation (1) [33].

$$D = \frac{0.94\lambda}{\beta \mathrm{Cos}\theta} \quad (1)$$

Where D is the crystallite size, K the shape factor, the wavelength, the diffraction angle and is the full width at half maximum (FWHM). However, the peak intensity decreased slightly with the increasing Ni^{2+} and Co^{2+} doping (Fig. 3(b)), indicating magnification in the crystallite size of the 3% Ni^{2+}, Co^{2+} doped sample. This was further confirmed by FWHM values at the $2\theta = 36.17, 37.25, 42.32, 43.46$ and $36.23, 37.28, 42.35, 43.46$ (Table 1) for 1% and 3% Ni^{2+} and Co^{2+} doped Bi_2O_3 samples, which decreased for the 3% Ni^{2+}, Co^{2+} doped Bi_2O_3 sample respectively. The two theta data obtained for more intense peaks can be assign to the reflection of (200), (114), (212), (115) hkl planes for the 2θ values mention earlier. According to the data obtained the JCPDS cart number 01-075-4627 match scan data is matches for the bismuth oxide nanoparticles with orthorhombic lattice and space group of Pbnb. Table 1 displayed the mean crystallite size of fabricated materials which was estimated by the FWHM of the XRD peaks using the Debye–Scherer equation. It can be seen from the table that the crystallite size was found to decrease with increasing the dopant concentration of Ni^{2+} and Co^{2+} respectively [34].

$ZnO\text{-}SnO_2\text{-}Zn_2SnO_4$

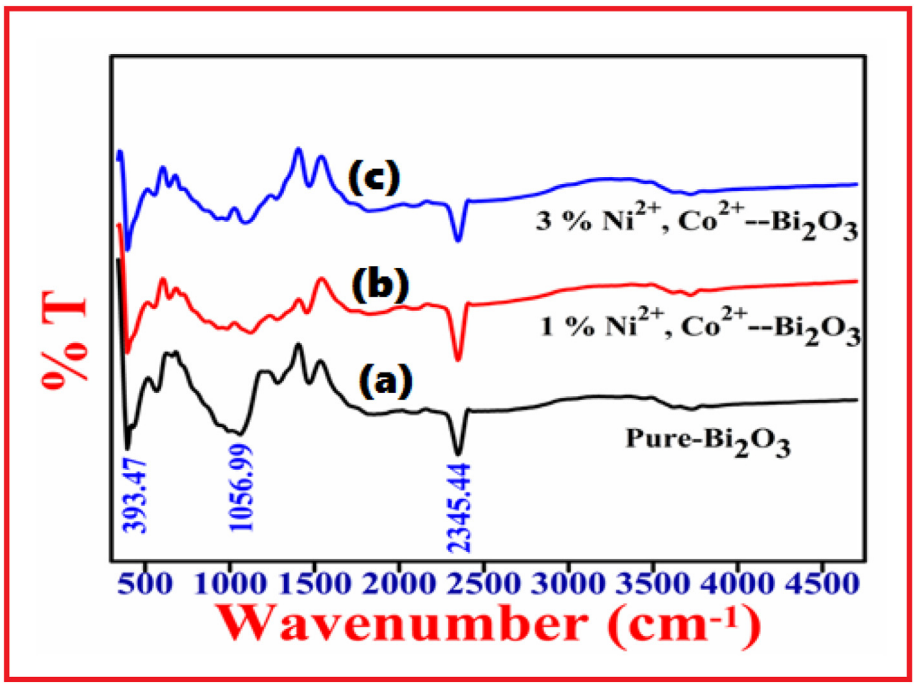

Fig. 7. (a) FT-IR spectra of bare Bi_2O_3, (b) 1% Co^{2+}, Ni^{2+} doped Bi_2O_3, (c) 3% Co^{2+}, Ni^{2+} doped Bi_2O.

3.3. Morphological study

The pure and Ni^{2+}, Co^{2+} doped Bi_2O_3 nanoparticles morphology were examined by FE-SEM analysis technique and the results are as shown in Fig. 4 (a)-(f). FE-SEM images of pure Bi_2O_3 nanoparticles (Fig. 4 (a)–(b)) point out toward the agglomeration occurred due the electrostatic attraction among the particles and shows irregular morphology of nanoparticles [35]. However, 1% Ni^{2+}, Co^{2+} doped Bi_2O_3 sample shows the highly compact nanorods like morphology with sharp edges (Fig. 4 (c)–(d)). While in case of 3% Ni^{2+}, Co^{2+} doped Bi_2O_3 sample revels the spherical morphology with highly rough surface area (Fig. 4 (e)–(f)). From the above observation of FE-SEM images of samples it can conclude that the $Ni^{2+}$and Co^{2+} induced the morphological changes in Bi_2O_3 nanoparticles as the concentration of dopant changes from 1% to 3%. Consequently, such alteration in the morphological structure of doped Bi_2O_3 nanoparticles provides large and rough surface area, which is essential for the effective photocatalytic applications [36].

Fig. 5, represents the TEM images of undoped and doped Bi_2O_3 nanoparticles. The crystal morphology, surface properties and nanoparticle dimensions can be examined from the study of transmission of electron microscopy. The TEM images and SAED pattern of undoped Bi_2O_3 nanoparticles is as shown in Fig. 5 (a)–(i), which shows the varied size of nanoparticles, agglomerated with almost spherical in dimensions. Figure c, f, i represents the selected area diffraction pattern (SAED) for undoped Bi_2O_3, the bright dark spots represents the crystalline nature of fabricated bismuth oxide nanoparticles. The dark bright rings appeared in the SAED pattern shows the polycrystalline nature of all the fabricated materials. Similarly, the TEM images of 1% Ni^{2+}, Co^{2+} doped Bi_2O_3 is as shown in figure d–e and 3% Ni^{2+}, Co^{2+} doped Bi_2O_3 is as shown in figure g–h. The images reveal the cubic arrangement of fabricated bismuth oxide nanoparticles. While the dark bright spot in SAED image of f and i indicating crystalline nature of 1% and 3% Ni^{2+}, Co^{2+} doped Bi_2O_3 nanoparticles. The TEM data obtained for bismuth oxide nanoparticles is in good agreement with the XRD and reported data [37,38].

3.4. Energy dispersive X-ray spectroscopy (EDS) study

To explore the exact elemental composition of synthesized undoped Bi_2O_3 and doped Bi_2O_3 samples were examine by the EDS analysis technique as shown in Fig. 6 (a)–(c). Fig. 6 (b)-(c) clearly indicates the exact elemental composition around the 1% Ni^{2+}, Co^{2+} doped Bi_2O_3 and 3% of Ni^{2+}, Co^{2+} doped Bi_2O_3 samples respectively. The EDS examination confirmed the successful synthesis of undoped Bi_2O_3 and doped Bi_2O_3 nanoparticles with no other addition peak, which reveals the purity of synthesized undoped Bi_2O_3 and doped Bi_2O_3 samples [39].

3.5. FT-IR analysis

The Fourier transform infrared spectrum (FT-IR) of the pure and doped Bi_2O_3 sample was analyzed and represented in Fig. 7. The metal oxide bonds are always lie in the range of 200–1000 cm^{-1} therefore, the low absorption vibration mode observed at wave number of 393.41 cm^{-1} due the presence of Bi-O bond of Bi_2O_3 [33]. While the absorption band around 1057 cm^{-1} is may be recognized due to the different type of vibration of Bi_2O_3 interactions. However, the absorption band observed at 2345.44 cm^{-1} is due the symmetrical and asymmetrical stretching frequency of CO_2 molecule absorbed from the atmosphere [40–42].

3.6. Brunauer-Emmett-Teller (BET) study

Surface area is an important parameter for the important applications such as surface adsorption like chemisorptions or physisorption. In the present study the prepared catalysts were subjected for BET study. The figure of BET N_2 adsorption-desorption curves for undoped Bi_2O_3, 1% Co^{2+}, Ni^{2+} doped Bi_2O_3, 3% Co^{2+}, Ni^{2+} doped Bi_2O_3 is as depicted in Fig. 8. While important parameters obtain from BET isotherm such as BET surface area (S_{BET}), pore volume (Vp), and pore diameter (Dp) is as represented in Table 2. The data mentioned in Table 1 confirms the surface of doped catalyst is enhanced in case of 1% Co^{2+}, Ni^{2+} doped Bi_2O_3, 3% Co^{2+}, Ni^{2+} doped Bi_2O_3. The surface area was observed to be 17.16 m^2/g, 60.86 m^2/g, 75.30 m^2/g for undoped Bi_2O_3, 1% Co^{2+}, Ni^{2+} doped Bi_2O_3, 3% Co^{2+}, Ni^{2+} doped Bi_2O_3adsorbents respectively. The

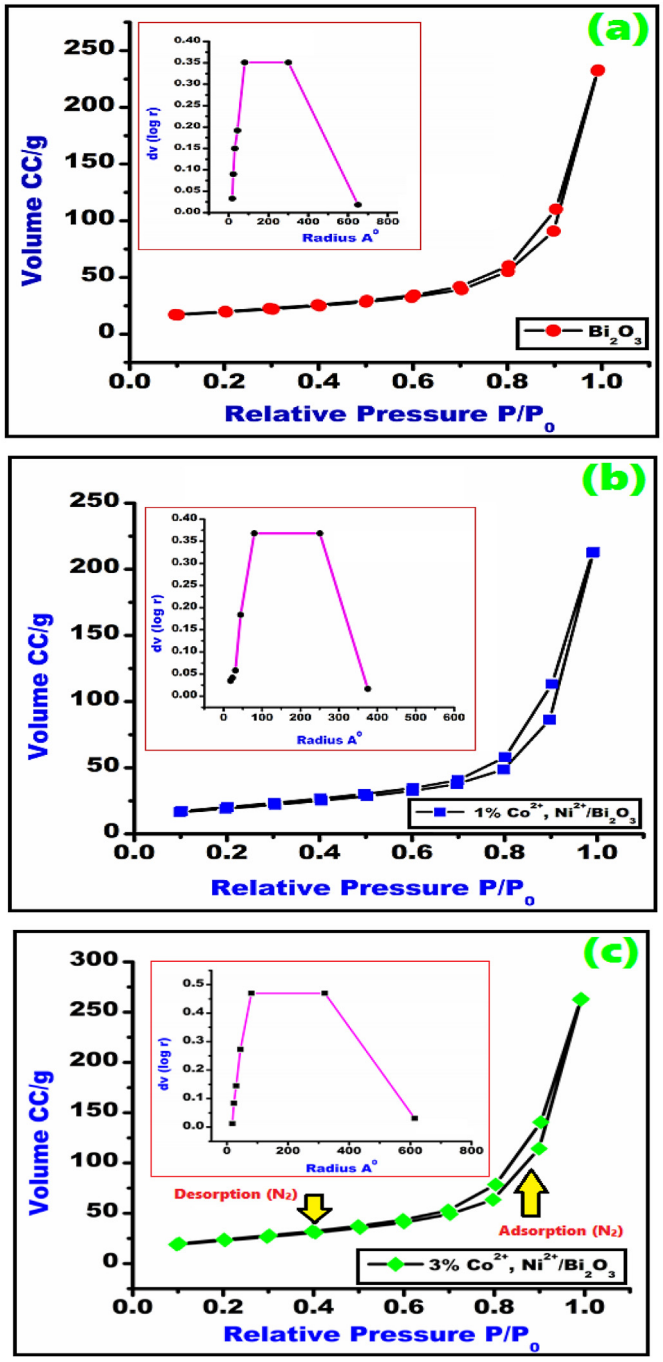

Fig. 8. BET N_2 adsorption-desorption curves a) bare Bi_2O_3, b) 1% Co^{2+}, Ni^{2+}doped Bi_2O_3, c) 3% Co^{2+}, Ni^{2+} doped Bi_2O_3 catalysts.

Table 2
BET surface area, pore volume, pore radius of undoped Bi_2O_3, 1% Co^{2+}, Ni^{2+} doped Bi_2O_3, 3% Co^{2+}, Ni^{2+} doped Bi_2O_3 catalysts.

Prepared Material	Surface Area (m^2/g)	Pore volume (cc/g)	Pore radius (Å)	R^2
Undoped Bi_2O_3	55.12	0.352	70.56	0.9992
1% Co^{2+}, Ni^{2+} doped Bi_2O_3	68.86	0.004	37.02	0.9999
3% Co^{2+}, Ni^{2+} doped Bi_2O_3	80.30	0.042	33.43	0.9999

probable reason for enhanced surface area in case of doped adsorbent is attributed to doping of more metal ion concentration in comparison to the undoped bismuth oxide adsorbent. During the catalysis study it also observed that due more surface area towards the 3% Co^{2+}, Ni^{2+} doped Bi_2O_3 the more dye was adsorbed on this catalysis and hence the degradation by this catalyst was maximum in contrast to the undoped Bi_2O_3 [43,44]. By drawing the isotherm, it is found that the isotherm belongs to type IV isotherm category with reference to the BDDT system which is a typical characteristic of porous materials.

3.7. Zeta potential report

In most of the chemical reactions, the surface charges are very provoking groups for the reactant to get active participation in the surface reactions. Since, surface reactions are proceeds via chemisorption or physisorption. Hence, both these phenomena are greatly influenced by surface charges over the smaller particles like nanoparticles in aqueous or any other media. Most of the nanoparticles can develop positive or negative charges due to their colloidal dispersion properties. The small positive or negative charges can be predicted by zeta potential report. The technique deals with the appropriate medium in which nanoparticles are present in the disperse medium. The techniques determine the minute charges present over the nanoparticles. According to research the charge present over the nanoparticles in turn gives stability of nanoparticles in the particular medium. Fig. 9 a-c showing the zeta potential report for undoped Bi_2O_3, 1% Co^{2+}, Ni^{2+}doped Bi_2O_3 and 3% Co^{2+}, Ni^{2+} doped Bi_2O_3 nanoparticles of −19.1 mV, 0.047 mV and −5.77 mV respectively. The variation in zeta potential digits affects the stability of bismuth oxide nanoparticles. The zeta potential values obtained for all the bismuth oxide nanoparticles implying their good stability in aqueous medium [45].

3.8. Ultra-violet diffuse reflectance spectroscopy (UV-DRS) study

The synthesized multi-doped Bi_2O_3 were subjected to UV-DRS. The spectra are given in Fig. 10. Shows appreciable activity in the UV-Vis range which is an important factor with respect to photocatalytic activity to harness large amount of light energy [46]. The undoped Bi_2O_3 shows highest absorption at 391 nm while Co^{2+} and Ni^{2+} shift the absorption maxima towards red shift. The 1% Co^{2+} and Ni^{2+} multi-doped Bi_2O_3 shows 428 nm and 3% Co^{2+} and Ni^{2+} concentration enable the material to absorb in the range of 447 nm which is attributed to the UV-vis absorption range [47]. The introduction of photosensitive dopants like Co and Ni improve the optical property of the Bi_2O_3 and it has affected the band gap energy of the synthesized materials. The band gap energy of the synthesized materials is calculated by equation (2) [48]. The yielded Tauc plots from all the UV-DRS spectra shows band gaps within the range of 2.35 to 2.20 eV and the minimum band gap energy is displayed by the 3% Co^{2+}, Ni^{2+} multi-doped Bi_2O_3 nanocrystalline material. The minimum band gap can be a significant factor to enhance the photocatalytic efficiency of the 3% multi-doped Bi_2O_3 since, more amount of electrons will produce thereby producing more number of ROS's in to the reaction mixture [49].

$$\alpha \cdot (h\nu) \cdot = C \cdot (h\nu - \cdot Eg)^{m/2} \quad (2)$$

Where, α is the absorption coefficient, $h\nu$ is photon energy in eV and C is constant. The of a Tauc's plot is the energy intercept of $(\alpha h\nu)^2$ vs. $h\nu$ gives Eg (Band gap energy) for direct transition (m=1).

4. Photocatalytic activity

The photocatalytic degradation of R-HCl dye was carried with the help of Quartz Glass Immersion photocatalytic reactor equipped with 400-W Mercury vapor lamp equiped with double jacket quartz immersion well, magnetic stirrer and chiller for water circulation and

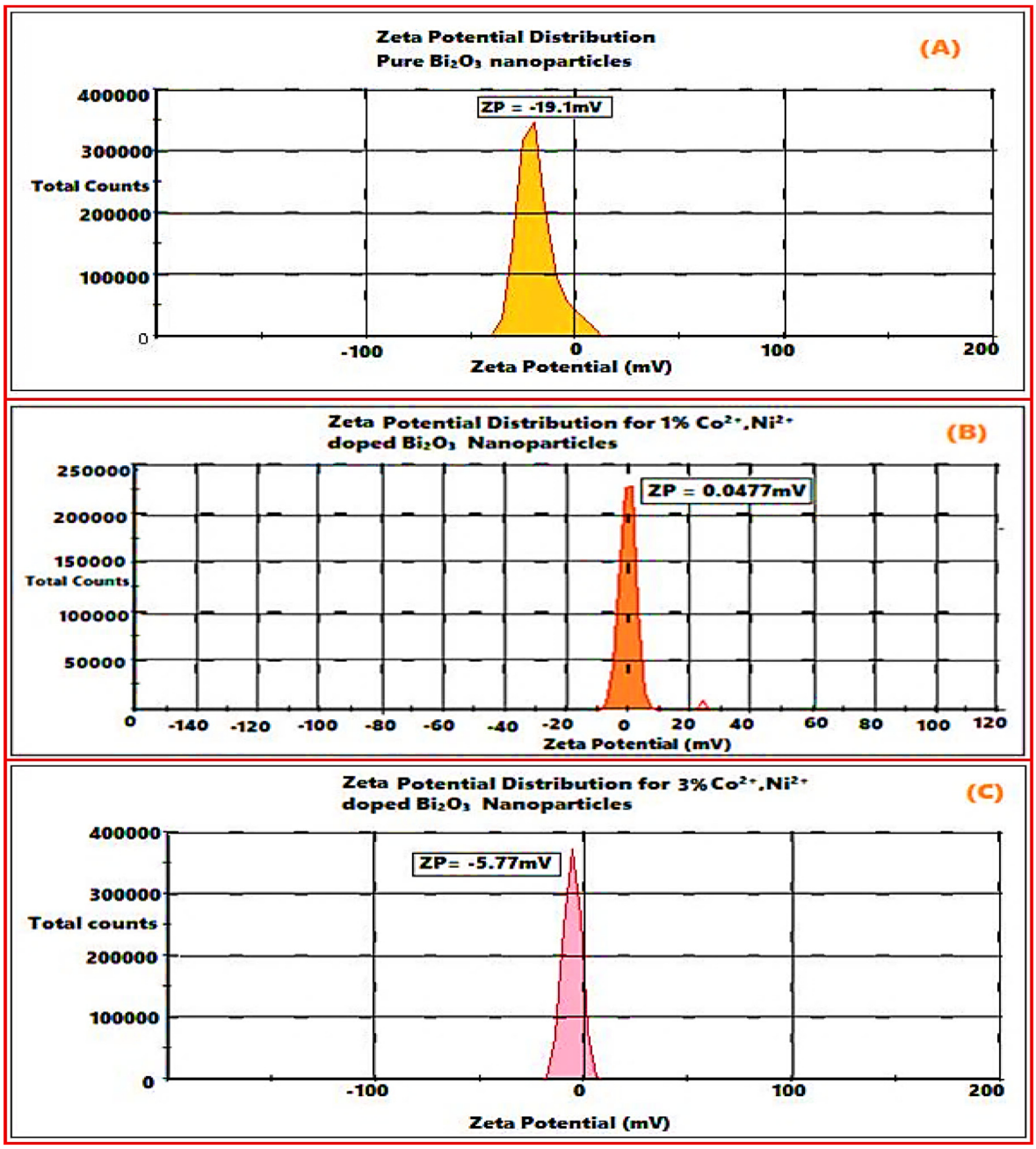

Fig. 9. Zeta potential Distribution curve of undoped Bi_2O_3 nanoparticles (a); 1% Ni^{2+}, Co^{2+} doped Bi_2O_3 nanoparticles (b); 3% Ni^{2+}, Co^{2+} doped Bi_2O_3 nanoparticles (c).

maintaining constant temperature. The overall changes in dye concentration were recorded with the help of Jasco V-730 Double beam spectrophotometer in the range of 300–800 nm. The pH of the photocatalytic experiment were adjusted and recorded with the assist of digital pH meter make Lab India equipped with a glass electrode. The pH meter was previously standardized with the help of buffer capsules of pH 4, 7, 9, and 12 ranging from acidic to the basic condition.

The photocatalytic degradation was calculated using the following equation (3).

$$\%D = \frac{Co - Ct}{Co} \text{X}100 \quad (3)$$

C_0 is initial concentration and C_t is the concentration at time t [50].

4.1. Effect of pH

The pH is one of the most important parameter to study the photocatalytic efficiency of the synthesized material. The pH controls surface reaction adsorption and generation of ROS in to the reaction mixture [51]. The undoped 3% multi-doped Bi_2O_3 was chosen for the detection of effect of pH on the photocatalytic degradation of R-HCl in aqueous phase. The pH was varied from 2 to 12 with the help of 0.1 N HCl and NaOH solution. The catalyst 0.3 mgL^{-1} catalyst was loaded and the mixture was then subjected to stirring for 1 h to attain the adsorption desorption equilibrium and subjected to visible light irradiation thereafter. The effect of pH was almost similar in case of both the catalyst however, R-HCl being a cationic dye certainly played an important role to show catalytic activity in the range of slightly higher pH (pH 8) as compared to the bare

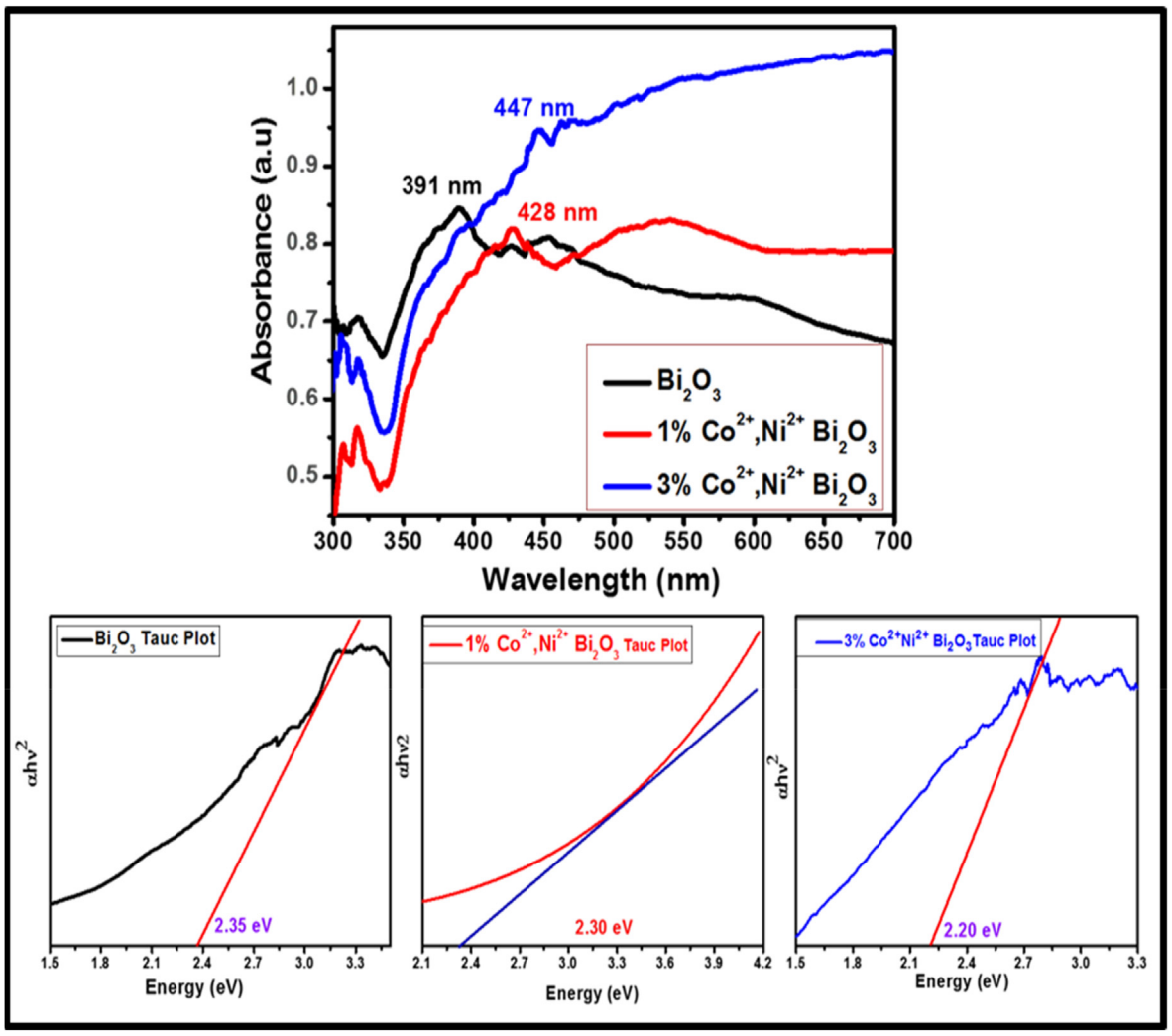

Fig. 10. UV-DRS followed by Tauc plots of bare Bi_2O_3, 1% Ni^{2+}, Co^{2+} doped Bi_2O_3 and 3% Ni^{2+}, Co^{2+} doped Bi_2O_3 nanoparticles.

Bi_2O_3. This is attributed to the charges on the catalytic surface since, the catalyst attain negative charge on the surface in acidic pH range the dye molecules got easily attracted towards the surface. The enhancement of these negative charges may be due to the presence of dopants in to the Bi_2O_3 crystal [52]. The combination of effective adsorption and photocatalysis overall increased the degaradtion capacity of the synthesized material in case of 3% multi-doped Bi_2O_3. The acidic pH favors the adsorption but restrict the generation of large amount of ROS in aqueous medium hence the pH around 7 to 8 favoured the photocatalytic degaradtion of R-HCl cationic dye [53,54]. The degaradtion efficiency of the multi-doped catalyst was greater than the undoped one at pH 8 and the pH range from slightly acidic then neutral to mild basic favours the degaradtion. However 3% multi-doped catalyst displayed higher efficiency at pH 8 attributed to the higher generation of ROS's which perform the function of degaradtion by photo Klobe reaction [55]. The effect of pH study is as depicted in Fig. 11.

4.2. Effect of initial dye concentarion

The influence of initial concentration of the dye for the degradation process is important and by carrying out the study one can calculate the initial rate of reaction and simultaneously rate constant of the reaction [56]. The initial dye concentrations of the R-HCl were varied in the range 10–40 mgL^{-1}. The degradation efficiency was found out to be inversely proportional to the initial dye concentration. The time–concentration profile for degradation of R-HCl is depicted in Fig. 12.

The rate of degradation decrease from 96 to 44% in 120 min as the initial dye concentration was increased from 10 to 40 mgL^{-1}. This observation is due to the interception of photon from light to reach the surface of catalyst, moreover the number of dye molecules increasing with concentration of dye have less number of active sites on catalyst surface and more of them are present in the bulk than on to the catalyst surface restrict the surface reactions as well as the penetration and increase the reflection of light [57,58]. The efficiency of the synthesized material especially the 3% multi-doped Bi_2O_3 is appreciable up to 30 mgL^{-1} in 120 min of irradiation.

4.3. Effect of catalyst dose

The photocatalytic activities of R-HCl with different multi-doped catalyst dosages are shown in Fig. 13. It is found that the catalytic activity of all the synthesized materials was directly proportional to the catalyst loading and the highest degradation was shown by 3% multi-doped catalyst. When the 3% Ni^{2+}, Co^{2+} doped Bi_2O_3 catalyst loading was 1 mgL^{-1} the efficiency was 68% and increased 96% at 4 mgL^{-1} further the catalytic efficiency remain fairly constant and no more remarkable activity was observed. This observation attributed to the increase in catalytic surface up to 4 mgL^{-1} and afterwards excess of catalyst leaded to the higher scattering rate of light due to the saturation of catalyst in the 100 ml dye solution [59–61]. The optimum catalyst

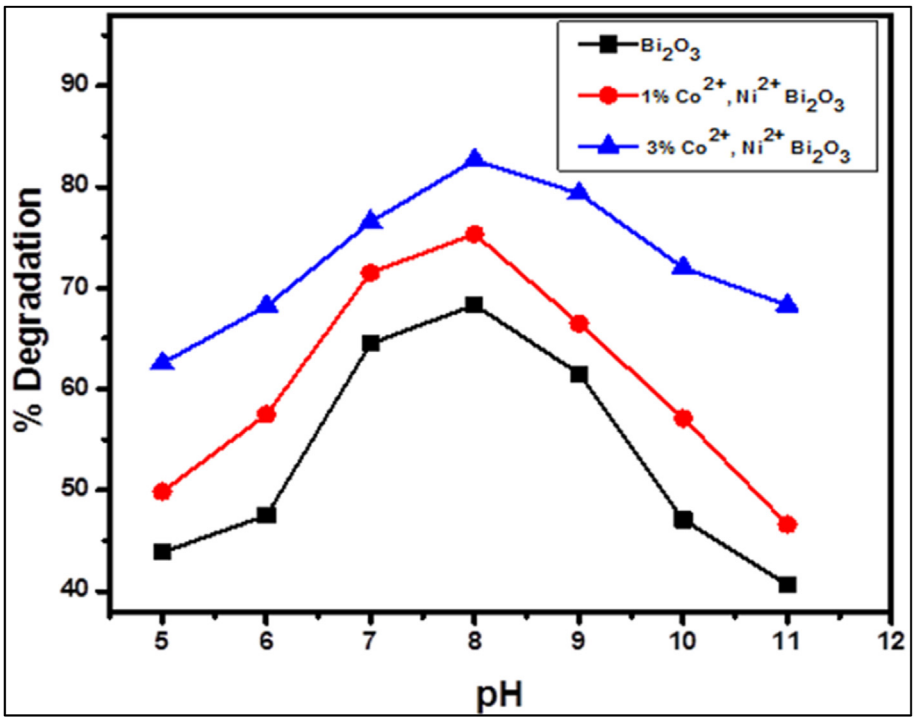

Fig. 11. Effect of pH on degradation of R-HCl by bare Bi_2O_3, 1% Ni^{2+}, Co^{2+} doped Bi_2O_3 nanoparticles and 3% Ni^{2+}, Co^{2+} doped Bi_2O_3 nanoparticles.

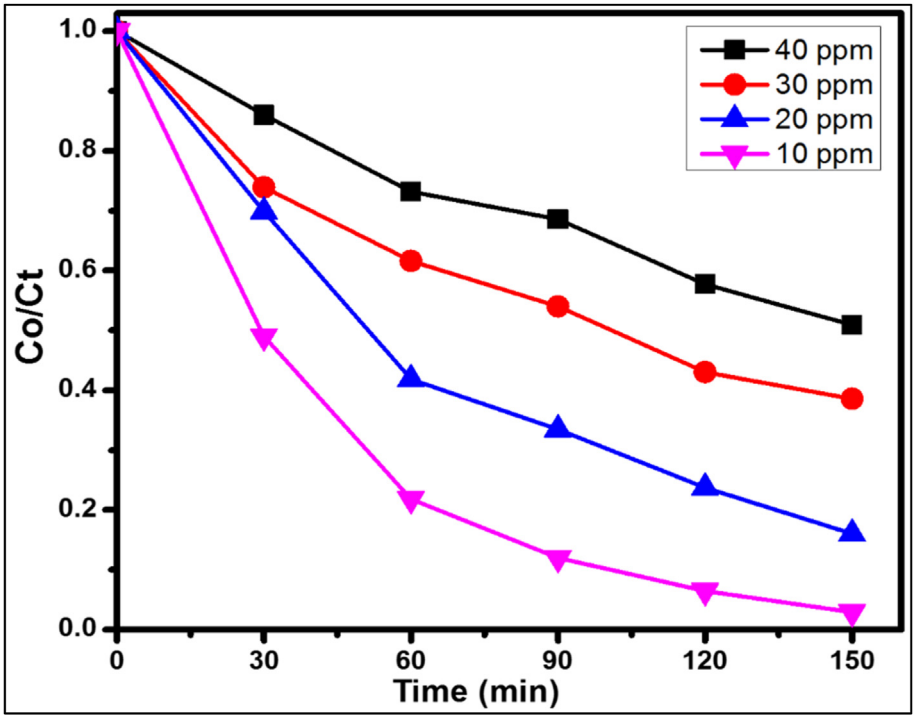

Fig. 12. Effect of dye concentration for the degradation of R-HCl by 3% Ni^{2+}, Co^{2+} doped Bi_2O_3 nanoparticles.

concentration for the degradation of 100 ml, 10 $mgL^{-1}$of pH 8 R-HCl solutions was 4 mgL^{-1} which is a minimum quantity and again increases the effectiveness of catalyst for large scale applications.

4.4. Comparision of nanocatalysts

The catalyst are compared for the degradation 100 ml of 10 mgL^{-1} dye with 4 mgL^{-1} bare and both multi-doped Bi_2O_3 catalyst loading at pH 8. The effect of comparison is depicted in Fig. 14 (a). The 3% nano-catalyst proved most effective in comparison. This is attributed to the generation of ample amount of ROS like $^{\cdot}OH$ and $O_2^{\cdot-}$ in the reaction assembly for the degradation of dye molecules. The generation of large number of electron and holes took place due to the addition of two dopants. The dopants do not allow to recombine with the holes [62–64]. The most effective catalyst for the complete degradation of R-HCl was 3% multi-doped Bi_2O_3 with contact time of 120 min attributed to its lower

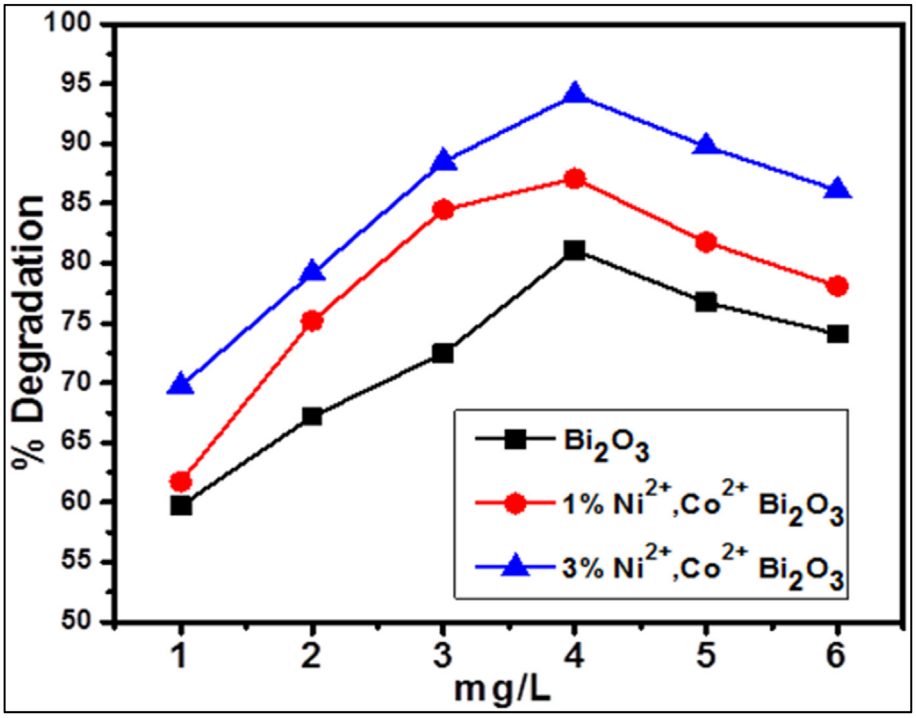

Fig. 13. Effect of catalyst dose for R-HCl degradation by bare Bi_2O_3, 1% Ni^{2+}, Co^{2+} doped Bi_2O_3 and 3% Ni^{2+}, Co^{2+} doped Bi_2O_3 nanoparticles.

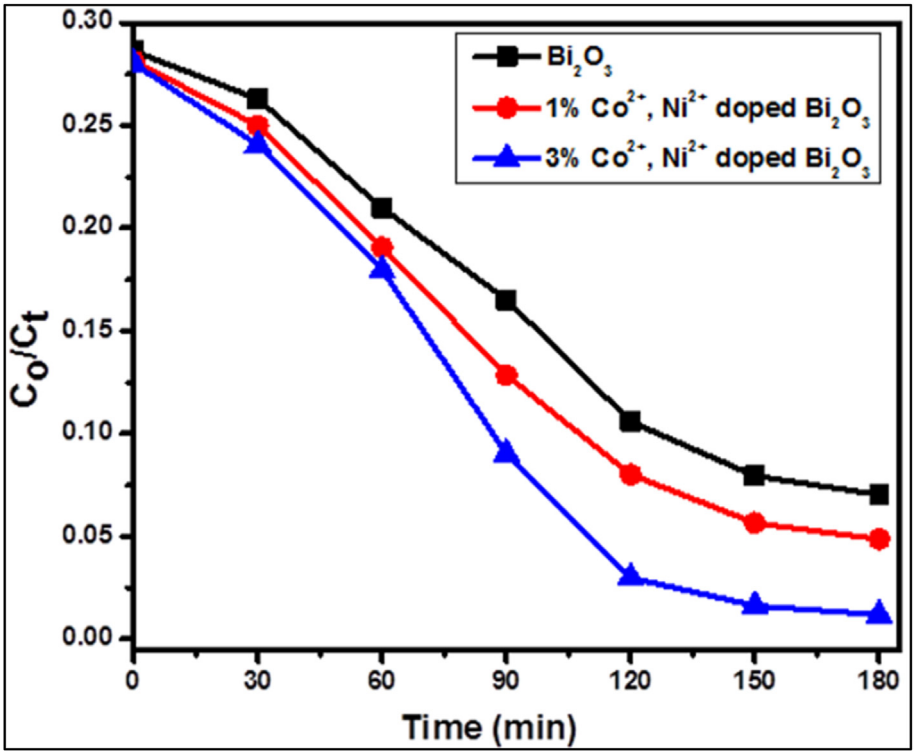

Fig. 14a. Effect of contact time on the degradation of R-HCl by bare Bi_2O_3, 1% and 3% Ni^{2+}, Co^{2+} doped Bi_2O_3 nanoparticles.

band gap energy and higher efficiency to absorb the light energy and generation of highly oxidizing ROS's which is fairly suitable for the economic and large scale point of view to perform efficient dye degradation process [65]. The continuous color fading of R-HCl dye by 3% multi-doped photocatalyst is given in Fig. 14 (b).

The reaction kinetics of R-HCl dye degradation was calculated using equation (4) [66].

$$\ln C_t / C_0 = kt \quad (4)$$

Where, C_0 is the initial dye concentration and C_t is the dye concentration at time t respectively. In Fig. 14 (c) the linear appearance of the plot of ln (C_t/C_0) (concentration ratio) vs the irradiation time (t) confirms the first-

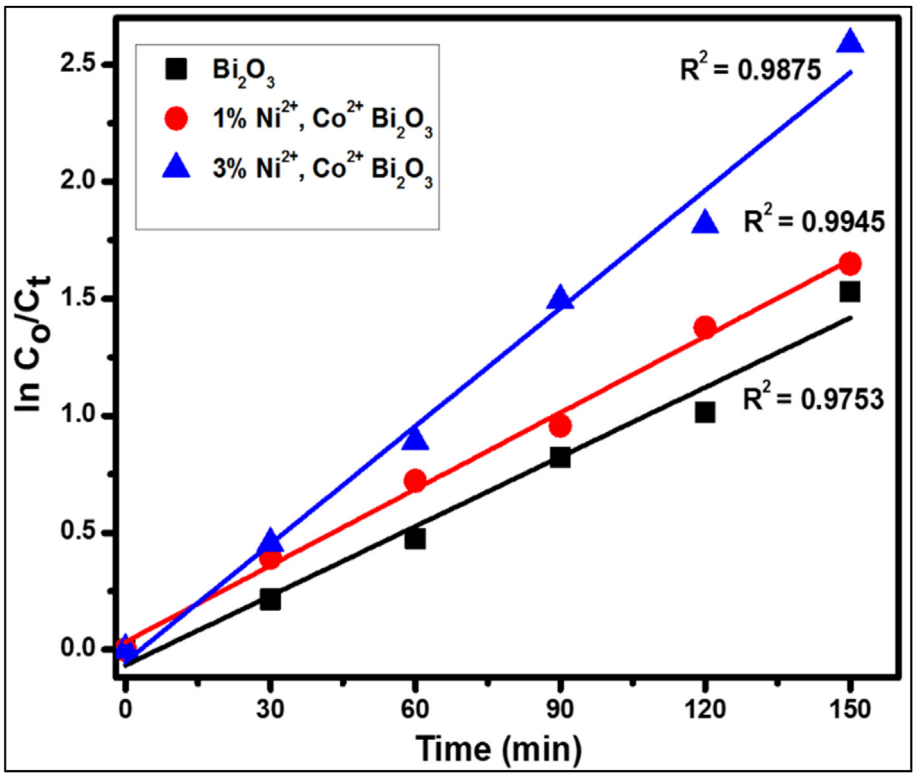

Fig. 14b. First-order rate kinetics for the degradation of R-HCl by bare Bi_2O_3, 1% and 3% Ni^{2+}, Co^{2+} doped Bi_2O_3 nanoparticles.

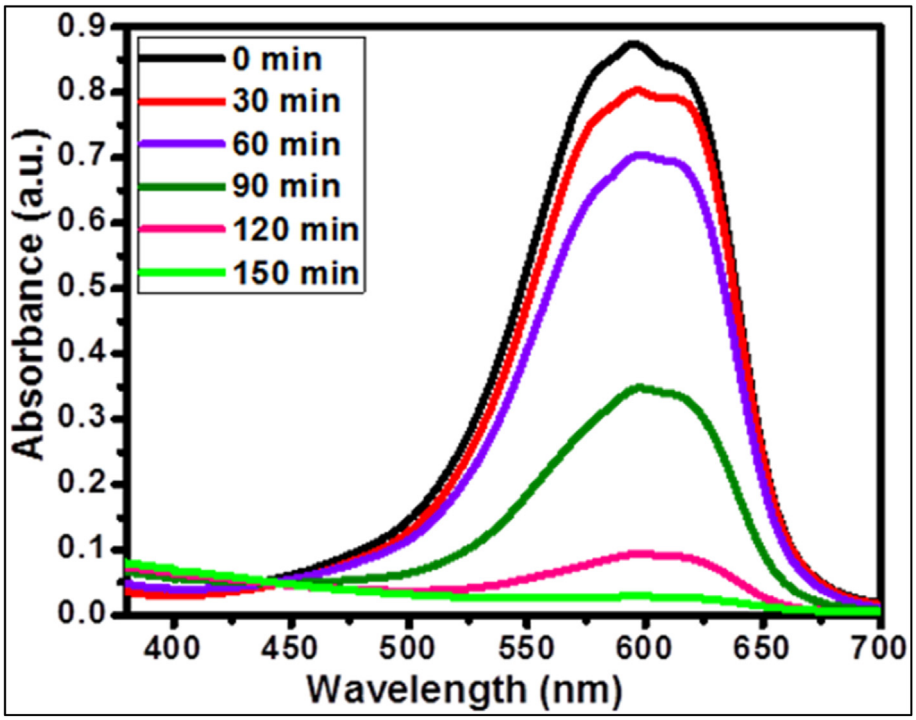

Fig. 14c. Continuous color fading of R-HCl by 3% Ni^{2+}, Co^{2+} doped Bi_2O_3 nanoparticles. (For interpretation of the references to color in this figure legend, the reader is referred to the Web version of this article.)

order rate kinetics of the R-HCl dye degradation. The rate constant K_a for bare Bi_2O_3, 1% and 3% Ni^{2+}, Co^{2+} doped Bi_2O_3 where found out 9.8×10^{-3}, 10.9×10^{-3} and 16.8×10^{-3} min^{-1} respectively confirming the efficiency of 3% nanocatalyst attributed to the percentage of transition metals [67,68]. The linear coefficient (R^2) of the three plots for R-HCl dye removal are 0.9753, 0.9945 and 0.9895 for bare, 1% and 3% Ni^{2+}, Co^{2+} Bi_2O_3 respectively. The R^2 value for the 3% multi-doped Bi_2O_3 indicate good fit and strong first-order reaction kinetics [69].

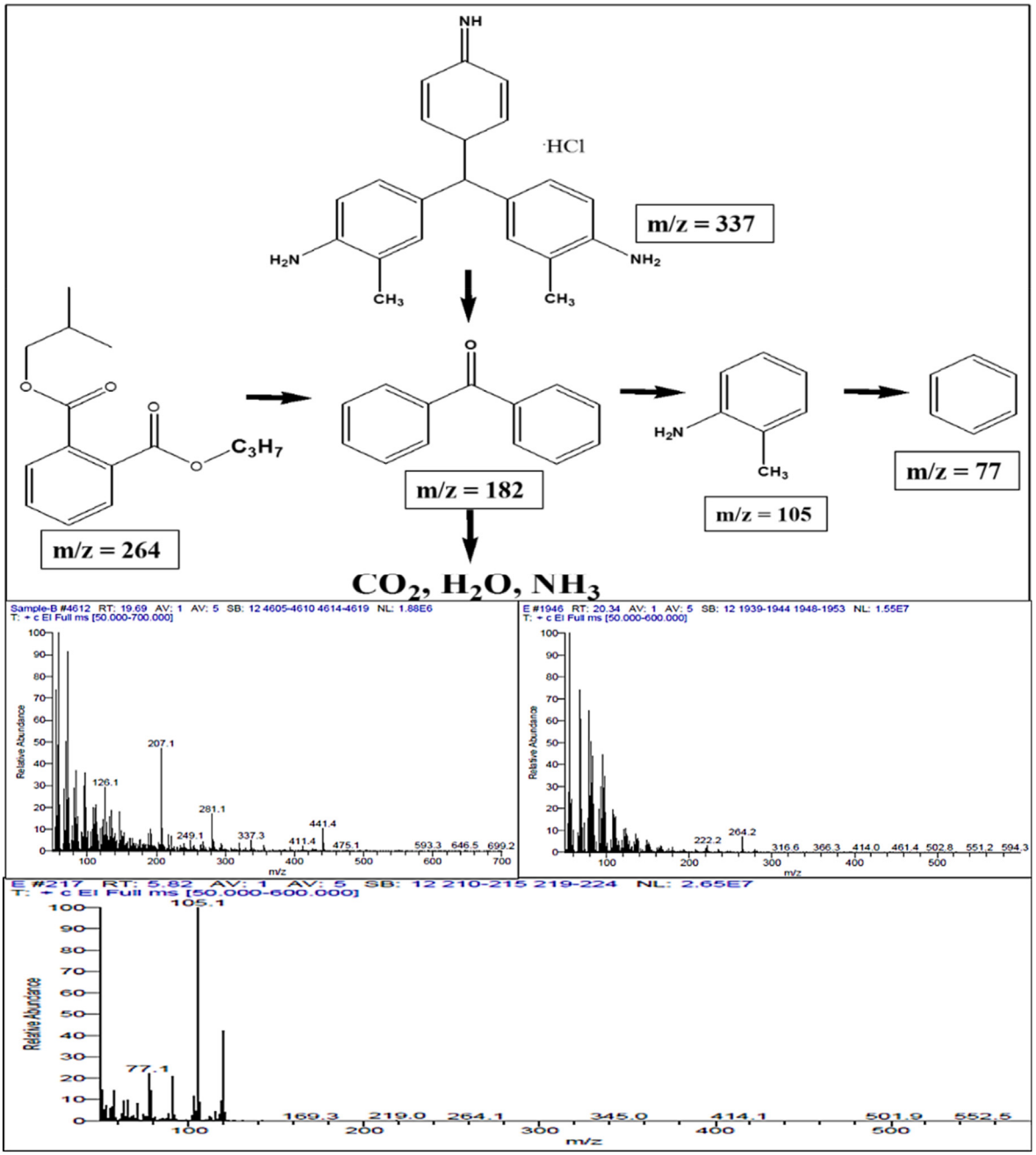

Fig. 15. LC-MS analysis of degraded Rosaniline dye sample by 3% Co^{2+}, Ni^{2+} doped Bi_2O_3 nanocatalyst.

4.5. LC-MS analysis of degraded dye sample

The analysis of degraded rosaniline dye sample was carried out to find degradation pathway of the dye molecules by LC-MS method. The degraded dye water solution was multi extracted in dichloro methane to transfer all the organic metabolites in organic phase. The extracted dichloro methane is then subjected to the LC-MS analysis [70]. The results obtain showed a lot of small molecular fragments in the LC-MS spectra confirmed the conversion of larger dye molecules in to smaller organic functionalities [71]. The larger mtabolites were present in smaller concentration again confirmed the efficient degradtion of rosaniline dye by the 3% Co^{2+}, Ni^{2+} doped Bi_2O_3 nanocatalyst. The fragments related to $m/z = 337$ confirms the dye molecule without fragmentation with highly oxidised $m/z = 264$ fragment depict the oxidation process by ROS. The $m/z = 182$, 105, 77 confirm bezopheneone, o-amino toluene and benzene formed during the degradation process eventually end up in to less toxic inorganic species like CO_2, H_2O and NH_3 [72,73]. The LC-MS analysis proves the efficient and highly oxidizing degradtion of the dye due to the highly generated ROS in the water samples. The LCMS analysis of degraded dye R-HCl is as depicted in Fig. 15.

4.6. Detection of ROS by scavenger addition

Reactive oxygen species like $^{\cdot}OH$, $O_2^{\cdot-}$ and h^+ participate in the photodegradation in AOP's. The exact effective ROS can be detected with the help of scavenger or quencher addition during the degradation process. Addition of isopropyl alcohol (IPA), benzoquinone (BQ) and EDTA to quench $^{\cdot}OH$, $O_2^{\cdot-}$ and h^+ respectively [74]. As evident in Fig. 16, when 1 mmol of IPA was added into the dye solution, the photodegradation efficiency was slightly decreased (8.5%) as compared to non-added solution however, after the addition of EDTA and BQ, especially EDTA the

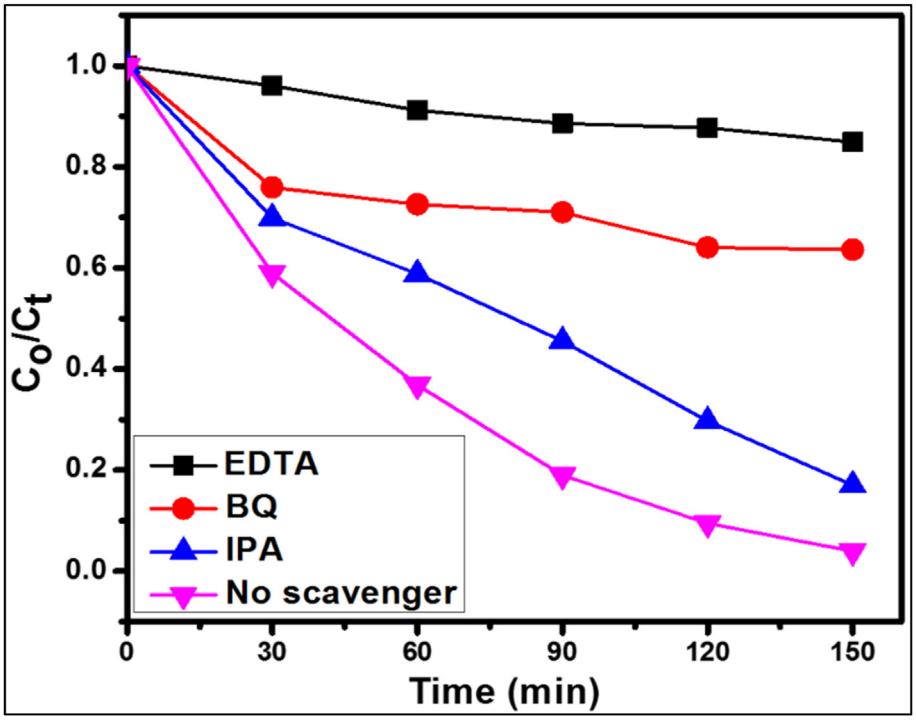

Fig. 16. Radical scavenging experiments for R-HCl dye degradation by 3% Ni^{2+}, Co^{2+} doped Bi_2O_3 nanocatalyst.

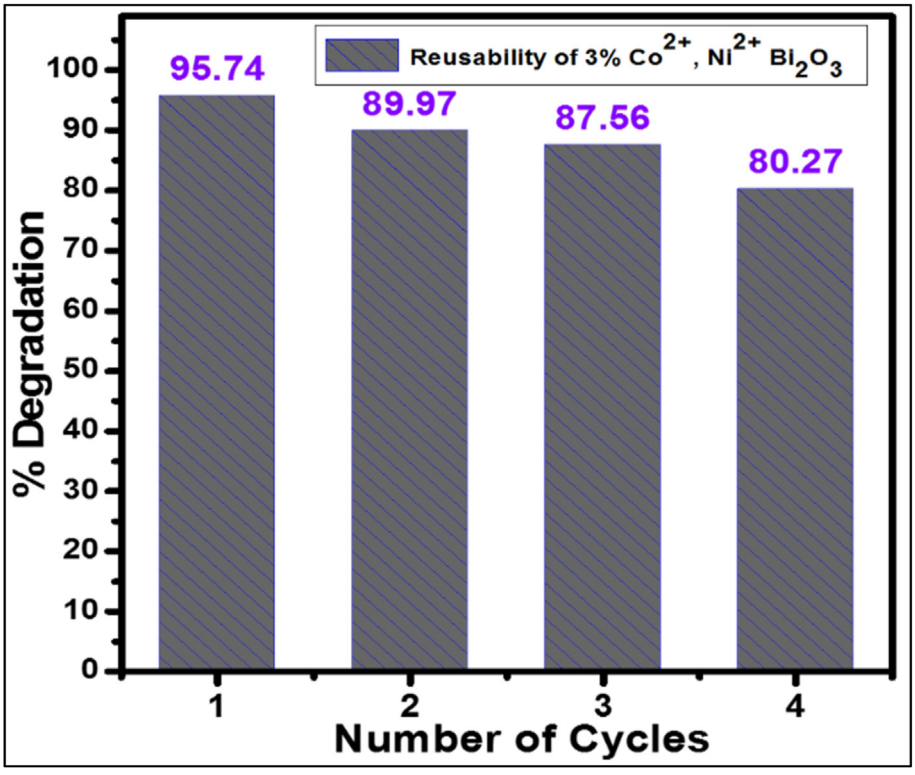

Fig. 17. Reusability of 3% Ni^{2+}, Co^{2+} doped Bi_2O_3 nanoparticles for R-HCl dye degradation.

photodegradation inhibited significantly 29.71% and 36.41% respectively for BQ and EDTA confirming O_2^- and h^+ the major ROS's in dye degradation [66,67]. The generation of electrons was the pivotal factor for the degradation of Rosaniline HCl dye by 3% Co^{2+}, Ni^{2+} doped Bi_2O_3 nanocatalyst. The diagrammatic presentation of radical scavenging experiment is as shown in Fig. 4.7.

4.7. Reusability study

The reusability of the catalyst was investigated for four cycles as mention in Fig. 17. After the first cycle the 3% Ni^{2+}, Co^{2+} doped Bi_2O_3 catalyst was filtered (after first cycle) with the help of Whatman filter paper 41, rinsed with ethanol and water from several time to eliminate

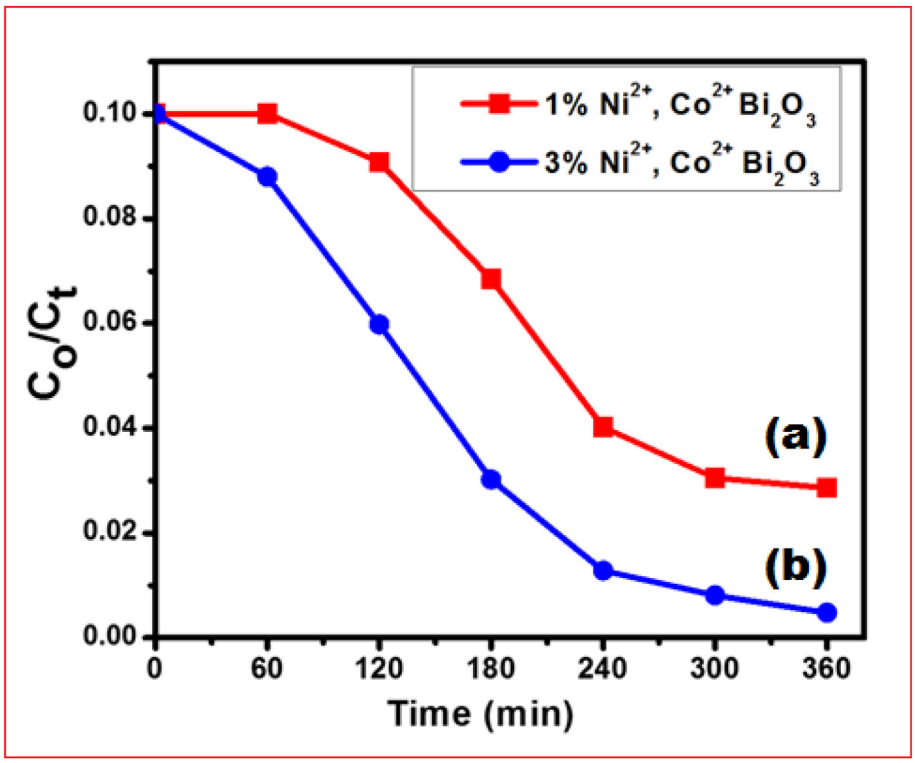

Fig. 18. (a) Phenol degradation study for 1% Ni^{2+}, Co^{2+} doped Bi_2O_3 nanoparticles, (b) 3% Ni^{2+}, Co^{2+} doped Bi_2O_3 nanoparticles.

adsorbed organic matter then dryed in an open air oven at 120 °C for 1h to eliminate organic impurities. Thereafter the catalyst was transformed in to the silicon crucible and heated in muffle furnace at 250 °C for 2 h. The catalyst recovered was subjected to multiple cycles repeating the procedure for the R-HCl dye degaradtion (100 ml dye solution, 10 mgL^{-1} initial dye concentarion and pH 8). The catalytic efficiency of synthesized nanomaterial decrease by almost 14% up to the fourth cycle which may be due to the loss of catalyst during filtration, decrease of active sites and surface area of the reused catalyst [75, 76].

4.8. Phenol degradation study

The fabricated catalysts 1% Ni^{2+}, Co^{2+} doped Bi_2O_3 and 3% Ni^{2+}, Co^{2+} doped Bi_2O_3 were employed for the degradation study of phenol molecule to investigate whether the molecule can be excited and degraded under visible light irradiation. The catalyst dose optimise was 30 mg/L, moderate pH of 7.5 and fixed catalyst loading under visible light irradiation. The phenol degradation curves for both the catalyst is as depicted in Fig. 18 a, b, showing very slow degradation of phenol molecule under UV visible irradiation with the contact time of almost 360 min. The slower degradation phenol molecule over the modified Bi_2O_3 is attributed to no successful quenching between phenol and fabricated catalysts molecules. In addition to this, the increased concentration of phenol leads to decrease in degradation efficiency due to accumulation phenol over the catalyst surface.

5. Conclusions

In summary it can be stated that the catalyst bare Bi_2O_3 was successfully fabricated by sol-gel route, while 1%, 3%, Co^{2+}, Ni^{2+} modified Bi_2O_3 material fabricated by co-precipitation method. The various characterization techniques reveal the successful fabrication of prepared catalysts. The ultimate use of the prepared catalysts in the wastewater treatment application proved that the synthesized materials have high efficiency for the photocatalytic degradation of cationic dye R-HCl. The low concentration of modified Bi_2O_3 was found to be very effective to degrade almost 97% of R-HCl dye at 30 mg L^{-1}, with slightly alkaline pH. By analysis technique it was observed that the high efficiency of modified Bi_2O_3 is due to enhanced surface area, excellent porosity and minimum band gap energy. These structural and surface modifications over modified Bi_2O_3 catalyst makes it an excellent photocatalysis that can be used in the photocatalytic degradation mechanisms for selected organic dyes. Thus, successful incorporation of transition metals Co^{2+}, Ni^{2+} over the Bi_2O_3 material is highly effective route to modify the metal oxide based semiconductors.

Funding information

The authors declared that they not received any grant from any funding agency for the present research work, the present work is self-funded.

Declaration of competing interest

Authors declared that they have no conflict of interest for the present research.

Acknowledgments

Authors are gratefully acknowledged to the SAIF-UDCT, Jalgaon (M.S) for XRD, SEM, EDS, IR, Zeta Potential studies. Authors are thankful to STIC Cochin University, Kerala for TEM analysis. Authors are grateful to SAIF, Savitribai Phule Pune University, Pune for BET and UV-DRS study. Authors are thankful to SAIF Chandigarh for LC-MS studies. Authors are very thankful to the Department of chemistry, MVP'S Arts, Commerce and Science College, Satana, District- Nashik for providing necessary laboratory facilities. Authors are also very much thankful to Authors are also grateful to Department of chemistry of, KVN ACS

College, Nashik, KTHM College, Nashik, GTP College, Nandurbar.

References

[1] Danish MSS, Estrella LL, Alemaida IMA, Lisin A, Moiseev N, Ahmadi M, Nazari M, Wali M, Zaheb H, Senjyu T. Photocatalytic applications of metal oxides for sustainable environmental remediation. Metals 2021;11(1):80. https://doi.org/10.3390/met11010080.

[2] Daghrir R, Drogui P, Robert D. Modified TiO_2 for environmental photocatalytic applications: a review. Ind. Eng. Chem. Res. 2013;13(52):3581–99. https://doi.org/10.1021/ie303468t. 10.

[3] Shekofteh-Gohari M, Habibi-Yangjeh A, Abitorabi M, Rouhi A. Magnetically separable nanocomposites based on ZnO and their applications in photocatalytic processes: a review. Crit. Rev. Environ. Sci. Technol. 2018;48(10–12):806–57. https://doi.org/10.1080/10643389.2018.1487227.

[4] Tang S, Wang Z, Yuan D, Zhang Y, Qi J, Rao Y, Lu G, Li B, Wang K, Yin K. Enhanced photocatalytic performance of $BiVO_4$ for degradation of methylene blue under LED visible light irradiation assisted by peroxymonosulfate. Int. J. Electrochem. Sci 2020;15(3):2470–80. https://doi.org/10.20964/2020.03.09.

[5] Lee KM, Lai CW, Ngai KS, Juan JC. Recent developments of zinc oxide based photocatalyst in water treatment technology: a review. Water Res. 2016;88:428–48. https://doi.org/10.1016/j.watres.2015.09.045.

[6] Kumar SG, Rao KK. Comparison of modification strategies towards enhanced charge carrier separation and photocatalytic degradation activity of metal oxide semiconductors (TiO_2, WO_3 and ZnO). Appl. Surf. Sci. 2017;391:124–48. https://doi.org/10.1016/j.apsusc.2016.07.081.

[7] Chan SH, Yeong WuT, Juan JC, The CY. Recent developments of metal oxide semiconductors as photocatalysts in advanced oxidation processes (AOPs) for treatment of dye waste-water. J. Chem. Technol. Biotechnol. 2011;86(9):1130–58. https://doi.org/10.1002/jctb.2636.

[8] Ajiboye TO, Oyewo OA, Onwudiwe DC. The performance of bismuth-based compounds in photocatalytic applications. Surf. Interface 2021;8:100927. https://doi.org/10.1016/j.surfin.2021.100927.

[9] Selvamani T, Anandan S, Granone L, Bahnemann DW, Ashokkumar M. Phase-controlled synthesis of bismuth oxide polymorphs for photocatalytic applications. Mater. Chem. Front. 2018;2(9):1664–73. https://doi.org/10.1039/C8QM00221E.

[10] Wang J, Li H, Yan X, Qian C, Xing Y, Yang S, Kang Z, Han J, Gu W, Yang H, Xiao F. Synergistic enhancement of the visible-light photocatalytic activity of hierarchical 3D $BiOCl_xBr_{1-x}$/graphene oxide heterojunctions for formaldehyde degradation at room temperature. J. Alloys Compd. 2019;795:120–33. https://doi.org/10.1016/j.jallcom.2019.04.176.

[11] Lin S, Du W, Tong L, Ji T, Jiao X. Photocatalytic degradation of 4-chlorophenol by Gd-doped β-Bi_2O_3 under visible light irradiation. Chem. Res. Chin. Univ. 2019;35(1):120–4. https://doi.org/10.1007/s40242-018-8170-6.

[12] Lan Y, Li Z, Li D, Xie W, Yan G, Guo S. Visible-light responsive Z-scheme Bi@β-Bi_2O_3/g-C_3N_4 heterojunction for efficient photocatalytic degradation of 2, 3-dihydroxynaphthalene. Chem. Eng. J. 2020;392:123686. https://doi.org/10.1016/j.cej.2019.123686.

[13] Zhang AY, He YY, Lin T, Huang NH, Xu Q, Feng JW. A simple strategy to refine Cu_2O photocatalytic capacity for refractory pollutants removal: roles of oxygen reduction and Fe (II) chemistry. J. Hazard Mater. 2017;330:9–17. https://doi.org/10.1016/j.jhazmat.2017.01.051.

[14] Nemiwal M, Zhang TC, Kumar D. Recent progress in g-C_3N_4, TiO_2 and ZnO based photocatalysts for dye degradation: strategies to improve photocatalytic activity. Sci. Total Environ. 2021;767:144896. https://doi.org/10.1016/j.scitotenv.2020.144896.

[15] Moradi H, Eshaghi A, Hosseini SR, Ghani K. Fabrication of Fe-doped TiO_2 nanoparticles and investigation of photocatalytic decolorization of reactive red 198 under visible light irradiation. Ultrason. Sonochem. 2016;32:314–9. https://doi.org/10.1016/j.ultsonch.2016.03.025.

[16] Liu L, Liu Z, Yang Y, Geng M, Zou Y, Shahzad MB, Dai Y, Qi Y. Photocatalytic properties of Fe-doped ZnO electrospun nanofibers. Ceram. Int. 2018;44(16):19998–20005. https://doi.org/10.1016/j.ceramint.2018.07.268.

[17] Sahoo DP, Rath D, Nanda B, Parida KM. Transition metal/metal oxide modified MCM-41 for pollutant degradation and hydrogen energy production: a review. RSC Adv. 2015;5(102):83707–24. https://doi.org/10.1039/C5RA14555D.

[18] Karthikeyan C, Arunachalam P, Ramachandran K, Al-Mayouf AM, Karuppuchamy S. Recent advances in semiconductor metal oxides with enhanced methods for solar photocatalytic applications. J. Alloys Compd. 2020;828:154281. https://doi.org/10.1016/j.jallcom.2020.154281.

[19] Fu F, Shen H, Xue W, Zhen Y, Soomro RA, Yang X, Wang D, Xu B, Chi R. Alkali-assisted synthesis of direct Z-scheme based Bi_2O_3/Bi_2MoO_6 photocatalyst for highly efficient photocatalytic degradation of phenol and hydrogen evolution reaction. J. Catal. 2019;375:399–409. https://doi.org/10.1016/j.jcat.2019.06.033.

[20] Medhi R, Marquez MD, Lee TR. Visible-light-active doped metal oxide nanoparticles: review of their synthesis, properties, and applications. ACS Appl. Nano Mater. 2020;3(7):6156–85. https://doi.org/10.1021/acsanm.0c01035.

[21] Shinde SG, Patil MP, Kim GD, Shrivastava VS. Ni, C, N, S multi-doped ZrO_2 decorated on multi-walled carbon nanotubes for effective solar induced degradation of anionic dye. J. Environ. Chem. Eng. 2020;8(3):103769. https://doi.org/10.1016/j.jece.2020.103769.

[22] Rani M, Shanker U. Photocatalytic degradation of toxic phenols from water using bimetallic metal oxide nanostructures. Colloid. Surface. Physicochem. Eng. Aspect. 2018;553:546–61. https://doi.org/10.1016/j.colsurfa.2018.05.071.

[23] Isac L, Cazan C, Enesca A, Andronic L. Copper sulfide based heterojunctions as photocatalysts for dyes photodegradation. Front. Chem. 2019;7:694. https://doi.org/10.3389/fchem.2019.00694.

[24] Dong S, Cui L, Liu C, Zhang F, Li K, Xia L, Su X, Feng J, Zhu Y, Sun J. Fabrication of 3D ultra-light graphene aerogel/Bi_2WO_6 composite with excellent photocatalytic performance: a promising photocatalyst for water purification. J. Taiwan Inst. Chem. Eng. 2019;97:288–96.

[25] Dong S, Cui L, Zhang W, Xia L, Zhou S, Russell CK, Fan M, Feng J, Sun J. Double-shelled $ZnSnO_3$ hollow cubes for efficient photocatalytic degradation of antibiotic wastewater. Chem. Eng. J. 2020;384:123279.

[26] Dong S, Cui L, Tian Y, Xia L, Wu Y, Yu J, Bagley DM, Sun J, Fan M. A novel and high-performance double Z-scheme photocatalyst ZnO-SnO_2-Zn_2SnO_4 for effective removal of the biological toxicity of antibiotics. J. Hazard Mater. 2020;399:123017.

[27] Dong S, Zhao Y, Yang J, Liu X, Li W, Zhang L, Wu Y, Sun J, Feng J, Zhu Y. Visible-light responsive PDI/rGO composite film for the photothermal catalytic degradation of antibiotic wastewater and interfacial water evaporation. Appl. Catal. B Environ. 2021;291:120127.

[28] Dong S, Xia L, Chen X, Cui L, Zhu W, Lu Z, Sun J, Fan M. Interfacial and electronic band structure optimization for the adsorption and visible-light photocatalytic activity of macroscopic ZnSnO3/graphene aerogel. Compos. B Eng. 2021;215:108765.

[29] Basaleh AS, Shawky A, Zaki ZI. Visible light-driven photodegradation of ciprofloxacin over sol-gel prepared Bi_2O_3-modified La-doped $NaTaO_3$ nanostructures. Ceram. Int. 2021;47(13):19205–12. https://doi.org/10.1016/j.ceramint.2021.03.268.

[30] Ozugurlu E. Cd-doped ZnO nanoparticles: an experimental and first-principles DFT studies. J. Alloys Compd. 2021;861:158620. https://doi.org/10.1016/j.jallcom.2021.158620.

[31] Siddiqui VU, Ansari A, Chauhan R, Siddiqi WA. Green synthesis of copper oxide (CuO) nanoparticles by Punica granatum peels extract. Mater. Today: Proc. 2021;36:751–5. https://doi.org/10.1016/j.matpr.2020.05.504.

[32] Bhatia S, Verma N. Photocatalytic activity of ZnO nanoparticles with optimization of defects. Mater. Res. Bull. 2017;95:468–76. https://doi.org/10.1016/j.materresbull.2017.08.019.

[33] Dinesh GK, Anandan S, Sivasankar T. Synthesis of Fe-doped Bi_2O_3 nanocatalyst and its sonophotocatalytic activity on synthetic dye and real textile wastewater. Environ. Sci. Pollut. Control Ser. 2016;23(20):20100–10. https://10.1007/s11356-015-5951-z.

[34] Kaur G, Sharma S, Kaur K, Bansal P. Synthesis, characterization, and visible-light-induced photocatalytic activity of powdered semiconductor oxides of bismuth and zinc toward degradation of Alizarin Red S. Water Environ. Res. 2020;92(9):1376–87. https://doi.org/10.1002/wer.1333.

[35] Koli PB, Kapadnis KH, Deshpande UG, Patil MR. Fabrication and characterization of pure and modified Co_3O_4 nanocatalyst and their application for photocatalytic degradation of eosine blue dye: a comparative study. J. Nanostruct. Chem. 2018;8(4):453–63. https://doi.org/10.1007/s40097-018-0287-0.

[36] Kumari P, Das RK, Pal B. Preparation and characterization of phase pure monoclinic α-Bi_2O_3 nanoparticles and influence of Ni^{2+} and Cu^{2+} impregnation on their photocatalytic properties. Mater. Chem. Phys. 2021;260:124173. https://doi.org/10.1016/j.matchemphys.2020.124173.

[37] Bera KK, Majumdar R, Chakraborty M, Bhattacharya SK. Phase control synthesis of α, β and α/β Bi_2O_3 hetero-junction with enhanced and synergistic photocatalytic activity on degradation of toxic dye, Rhodamine-B under natural sunlight. J. Hazard Mater. 2018;15(352):182–91. https://doi.org/10.1016/j.jhazmat.2018.03.029.

[38] Munir S, Rasheed A, Zulfiqar S, Aadil M, Agboola PO, Shakir I, Warsi MF. Synthesis, characterization and photocatalytic parameters investigation of a new $CuFe_2O_4$/Bi_2O_3 nanocomposite. Ceram. Int. 2020;46(18):29182–90. https://doi.org/10.1016/j.ceramint.2020.08.091.

[39] Jothibas M, Manoharan C, Jeyakumar SJ, Praveen P. Study on structural and optical behaviors of In_2O_3 nanocrystals as potential candidate for optoelectronic devices. J. Mater. Sci. Mater. Electron. 2015;26(12):9600–6. https://doi.org/10.1007/s10854-015-3623-x.

[40] Najim AA. Synthesis and characterizations of (δ-Bi_2O_3) 0.93 (TiO_2) 0.07 thin films grown by PLD technique for optoelectronics. Mater. Sci. Semicond. Process. 2017;71:378–81. https://doi.org/10.1016/j.mssp.2017.08.035.

[41] Koli PB, Kapadnis KH, Deshpande UG, Tupe UJ, Shinde SG, Ingale RS. Fabrication of thin film sensors by spin coating using sol-gel $LaCrO_3$ Perovskite material modified with transition metals for sensing environmental pollutants, greenhouse gases and relative humidity. Environ. Challenges 2021;3:100043. https://doi.org/10.1016/j.envc.2021.100043.

[42] Waghchaure RH, Koli PB, Adole VA, Jagdale BS. Transition metals Ni^{2+}, Fe^{3+} incorporated modified ZnO thick film sensors to monitor the environmental and industrial pollutant gases. Orient. J. Chem. 2020;36(6):1049–65. https://doi.org/10.13005/ojc/360607.

[43] Hou J, Wang Z, Jiao S, Zhu H. Bi_2O_3 quantum-dot decorated nitrogen-doped Bi_3NbO_7 nanosheets: in situ synthesis and enhanced visible-light photocatalytic activity. CrystEngComm 2012;14(18):5923–8. https://doi.org/10.1039/C2CE25504A.

[44] Zhou T, Hu J, Li J. Er^{3+} doped bismuth molybdate nanosheets with exposed {0 1 0} facets and enhanced photocatalytic performance. Appl. Catal. B Environ. 2011;110:221–30. https://doi.org/10.1016/j.apcatb.2011.09.004.

[45] Shinde SG, Shrivastava VS. Ni and Zn modified acid activated montmorillonite clay for effective removal of carbol fuchsin dye from aqueous solution. SN Appl. Sci. 2020;2(4):1–11. https://doi.org/10.1007/s42452-020-2295-1.

[46] Peng M, Zhang N, Wondraczek L, Qiu J, Yang Z, Zhang Q. Ultrabroad NIR luminescence and energy transfer in Bi and Er/Bi co-doped germanate glasses. Opt Express 2011;19(21):20799–807. https://doi.org/10.1364/OE.19.020799.
[47] Nguyen Thi Thu T, Nguyen Thi N, Tran Quang V, Nguyen Hong K, Nguyen Minh T, Le Thi Hoai N. Synthesis, characterisation, and effect of pH on degradation of dyes of copper-doped TiO_2. J. Exp. Nanosci. 2016;11(3):226–38. https://doi.org/10.1080/17458080.2015.1053541.
[48] Sahoo C, Gupta AK, Sasidharan Pillai IM. Photocatalytic degradation of methylene blue dye from aqueous solution using silver ion-doped TiO_2 and its application to the degradation of real textile wastewater. J. Environ. Sci. Health, A 2012;47(10):1428–38. https://doi.org/10.1080/10934529.2012.672387.
[49] Saquib M, Muneer M. Photocatalytic degradation of two selected textile dye derivatives, eosine yellowish and p-rosaniline, in aqueous suspensions of titanium dioxide. J. Environ. Sci. Health, A 2003;38(11):2581–98. https://doi.org/10.1081/ESE-120024448.
[50] Mahmoodi NM, Arami M. Degradation and toxicity reduction of textile wastewater using immobilized titania nanophotocatalysis. J. Photochem. Photobiol. B Biol. 2009;94(1):20–4. https://doi.org/10.1016/j.jphotobiol.2008.09.004.
[51] Swaminathan K, Sandhya S, Sophia AC, Pachhade K, Subrahmanyam YV. Decolorization and degradation of H-acid and other dyes using ferrous–hydrogen peroxide system. Chemosphere 2003;50(5):619–25. https://doi.org/10.1016/S0045-6535(02)00615-X.
[52] Khairnar SD, Patil MR, Shrivastava VS. Hydrothermally synthesized nanocrystalline Nb_2O_5 and its visible-light photocatalytic activity for the degradation of Congo red and methylene blue. Iran. J. Catal. 2018;8(2):143–50.
[53] Medina JC, Portillo-Vélez NS, Bizarro M, Hernández-Gordillo A, Rodil SE. Synergistic effect of supported ZnO/Bi_2O_3 heterojunctions for photocatalysis under visible light. Dyes Pigments 2018;153:106–16. https://doi.org/10.1016/j.dyepig.2018.02.006.
[54] Hu L, Zhang G, Liu M, Wang Q, Wang P. Enhanced degradation of Bisphenol A (BPA) by peroxymonosulfate with Co_3O_4-Bi_2O_3 catalyst activation: effects of pH, inorganic anions, and water matrix. Chem. Eng. J. 2018;338:300–10. https://doi.org/10.1016/j.cej.2018.01.016.
[55] Khairnar SD, Kulkarni AN, Shinde SG, Marathe SD, Marathe YV, Dhole SD, Shrivastava VS. Synthesis and characterization of 2-D La-doped Bi_2O_3 for photocatalytic degradation of organic dye and pesticide. J. Photochem. Photobiol., A 2021;6:100030. https://doi.org/10.1016/j.jpap.2021.100030.
[56] Nguyen CH, Fu CC, Juang RS. Degradation of methylene blue and methyl orange by palladium-doped TiO_2 photocatalysis for water reuse: efficiency and degradation pathways. J. Clean. Prod. 2018;202:413–27. https://doi.org/10.1016/j.jclepro.2018.08.110.
[57] Kritikos DE, Xekoukoulotakis NP, Psillakis E, Mantzavinos D. Photocatalytic degradation of reactive black 5 in aqueous solutions: effect of operating conditions and coupling with ultrasound irradiation. Water Res. 2007;41(10):2236–46. https://doi.org/10.1016/j.watres.2007.01.048.
[58] Subash B, Krishnakumar B, Swaminathan M, Shanthi M. Highly efficient, solar active, and reusable photocatalyst: Zr-loaded Ag–ZnO for reactive red 120 dye degradation with synergistic effect and dye-sensitized mechanism. Langmuir 2013;29(3):939–49. https://doi.org/10.1021/la303842c.
[59] Koli PB, Kapadnis KH, Deshpande UG. Transition metal decorated Ferrosoferric oxide (Fe_3O_4): an expeditious catalyst for photodegradation of Carbol Fuchsin in environmental remediation. J. Environ. Chem. Eng. 2019;7(5):103373. https://doi.org/10.1016/j.jece.2019.103373.
[60] Jamil A, Bokhari TH, Javed T, Mustafa R, Sajid M, Noreen S, Zuber M, Nazir A, Iqbal M, Jilani MI. Photocatalytic degradation of disperse dye Violet-26 using TiO_2 and ZnO nanomaterials and process variable optimization. J. Mater. Res. Technol. 2020;9(1):1119–28. https://doi.org/10.1016/j.jmrt.2019.11.035.
[61] Ashraf SS, Rauf MA, Alhadrami S. Degradation of Methyl Red using Fenton's reagent and the effect of various salts. Dyes Pigments 2006;69(1–2):74–8. https://doi.org/10.1016/j.dyepig.2005.02.009.
[62] Daneshvar N, Aleboyeh A, Khataee AR. The evaluation of electrical energy per order (EEo) for photooxidative decolorization of four textile dye solutions by the kinetic model. Chemosphere 2005;59(6):761–7.
[63] Balachandran S, Swaminathan M. Facile fabrication of heterostructured Bi_2O_3–ZnO photocatalyst and its enhanced photocatalytic activity. J. Phys. Chem. C 2012;116(50):26306–12. https://doi.org/10.1021/jp306874z. 20.
[64] Shinde SG, Patil MP, Kim GD, Shrivastava VS. Multi-doped ZnO photocatalyst for solar induced degradation of indigo carmine dye and as an antimicrobial agent. J. Inorg. Organomet. Polym. Mater. 2020;30(4):1141–52. https://doi.org/10.1007/s10904-019-01273-2.
[65] Andersen WC, Turnipseed SB, Karbiwnyk CM, Lee RH, Clark SB, Rowe WD, Madson MR, Miller KE. Multiresidue method for the triphenylmethane dyes in fish: malachite green, crystal (gentian) violet, and brilliant green. Anal. Chim. Acta 2009;1(1–2):279–89. https://doi.org/10.1016/j.aca.2008.09.041. 637.
[66] Ahmed T, Noman M, Shahid M, Niazi MB, Hussain S, Manzoor N, Wang X, Li B. Green synthesis of silver nanoparticles transformed synthetic textile dye into less toxic intermediate molecules through LC-MS analysis and treated the actual wastewater. Environ. Res. 2020;1(191):110142. https://doi.org/10.1016/j.envres.2020.110142.
[67] Yu K, Yang S, Boyd SA, Chen H, Sun C. Efficient degradation of organic dyes by $BiAg_xO_y$. J. Hazard Mater. 2011;197:88–96. https://doi.org/10.1016/j.jhazmat.2011.09.056.
[68] González B, Trujillano R, Vicente MA, Rives V, Korili SA, Gil A. Photocatalytic degradation of trimethoprim on doped Ti-pillared montmorillonite. Appl. Clay Sci. 2019;167:43–9. https://doi.org/10.1016/j.clay.2018.10.006.
[69] Straub R, Voyksner RD, Keever JT. Thermospray, particle beam and electrospray liquid chromatography-mass spectrometry of azo dyes. J. Chromatogr. A 1992;627(1–2):173–86. https://doi.org/10.1016/0021-9673(92)87197-G.
[70] Pelaez M, Falaras P, Likodimos V, O'Shea K, Armah A, Dunlop PS, Byrne JA, Dionysiou DD. Use of selected scavengers for the determination of NF-TiO_2 reactive oxygen species during the degradation of microcystin-LR under visible light irradiation. J. Mol. Catal. Chem. 2016;425:183–9. https://doi.org/10.1016/j.molcata.2016.09.035.
[71] Wang W, Fang HB, Zheng YZ, Che Y, Tao X, Chen JF. In situ template-free synthesis of a novel 3D p–n heteroarchitecture Ag_3PO_4/Ta_3N_5 photocatalyst with high activity and stability under visible radiation. RSC Adv. 2015;5(77):62519–26. https://doi.org/10.1039/C5RA10771G.
[72] Ong CB, Ng LY, Mohammad AW. A review of ZnO nanoparticles as solar photocatalysts: synthesis, mechanisms and applications. Renew. Sustain. Energy Rev. 2018;81:536–51. https://doi.org/10.1016/j.rser.2017.08.020.
[73] Zangeneh H, Farhadian M, Zinatizadeh AA. A reusable visible driven N and C–N doped TiO_2 magnetic nanocomposites for photodegradation of direct red 16 azo dye in water and wastewater. Environ. Technol. 2020:1–16. https://doi.org/10.1080/09593330.2020.1825530.
[74] Liu F, Sun Y, Gu J, Gao Q, Sun D, Zhang X, Pan B, Qian J. Highly efficient photodegradation of various organic pollutants in water: rational structural designs of photocatalyst via thiol-ene click reaction. Chem. Eng. J. 2020;381:122631.